Cell Reports

Article

CBP-IDRs regulate acetylation and gene expression

Graphical abstract

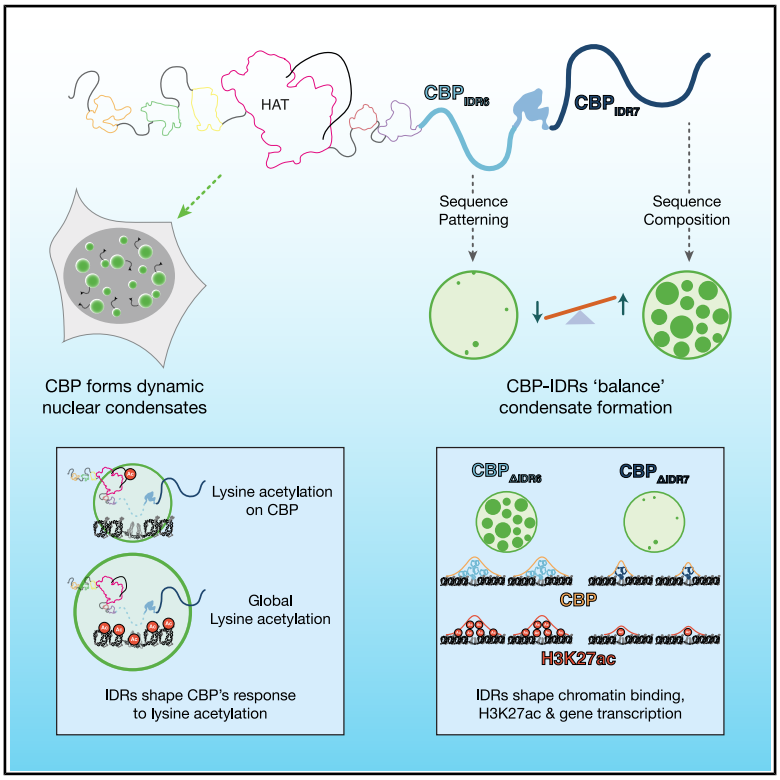

Authors

Katie L. Gelder, Nicola A. Carruthers, Grace Gilbert, ..., Timothy D. Craggs, Alison E. Twelvetrees, Daniel A. Bose

Correspondence

d.bose@sheffield.ac.uk

In brief

Gelder et al. demonstrate that intrinsically disordered regions (IDRs) with divergent sequence properties maintain a functional balance between positive and negative regulation of CBP condensates. This intramolecular mechanism tunes CBP's sensitivity to lysine acetylation; its disruption fundamentally alters chromatin binding, histone acetylation, and gene expression.

Highlights

- CBP-IDRs are critical regulators of diverse CBP functions
- C-terminal CBP-IDRs balance condensates through divergent sequence properties
- IDR-driven balance tunes how CBP condensates respond to global and direct lysine acetylation
- CBP-IDR disruption alters chromatin occupancy, histone acetylation, and gene transcription

Gelder et al., 2026, Cell Reports *45*, 117109
March 24, 2026
https://doi.org/10.1016/j.celrep.2026.117109

CellPress

Cell Reports

CellPress
OPEN ACCESS

Article

CBP-IDRs regulate acetylation and gene expression

Katie L. Gelder,[1,4] Nicola A. Carruthers,[1,4,7] Grace Gilbert,[1,4,5,11] Laura J. Harrison,[1,4,8,11] Brychan V. Evans,[1,4] Thomas I. Evans,[1] Sophie S. Ball,[1,9] Mark Dunning,[4,5,6,10] Timothy D. Craggs,[3,4] Alison E. Twelvetrees,[2,5] and Daniel A. Bose[1,4,12,13,*]

[1]Molecular and Cellular Biology, School of Biosciences, The University of Sheffield, Sheffield S10 2TN, UK
[2]Division of Neuroscience, The School of Medicine and Population Health, Faculty of Health, The University of Sheffield, Sheffield S10 2HQ, UK
[3]Department of Chemistry, School of Mathematical and Physical Sciences, Faculty of Science, The University of Sheffield, Sheffield S3 7HF, UK
[4]Nucleic Acids Institute, The University of Sheffield, Sheffield S10 2TN, UK
[5]Neuroscience Institute, The University of Sheffield, Sheffield S10 2AH, UK
[6]Sheffield Bioinformatics Core, Faculty of Health, The University of Sheffield, Sheffield S10 2HQ, UK
[7]Present address: MRC Human Genetics Unit, University of Edinburgh, Edinburgh, UK
[8]Present address: Max-Planck-Zentrum für Physik und Medizin, Erlangen, Germany
[9]Present address: Department of Immunology and Inflammation, Imperial College London, London, UK
[10]Present address: Department of Metabolism, Digestion and Reproduction, Imperial College London, London, UK
[11]These authors contributed equally
[12]Senior author
[13]Lead contact
*Correspondence: d.bose@sheffield.ac.uk
https://doi.org/10.1016/j.celrep.2026.117109

SUMMARY

Intrinsically disordered regions (IDRs) are essential regulators of protein function despite lacking stable secondary and tertiary structures. IDRs are integral to the function of multidomain regulatory proteins, such as the essential transcriptional coactivators *cAMP response element-binding protein* (CREB)-*binding protein* (CBP) and *EP300* (p300), but how their multiple IDRs work together to regulate function remains poorly understood. Here, we demonstrate that different CBP-IDRs cooperate to control complex nuclear behaviors. We show how CBP-IDRs with different sequence properties make unique contributions to CBP behavior, establishing a critical balance between positive and negative regulation of CBP condensates. These opposing interactions are functionally important, tuning CBP's sensitivity to regulatory cues such as lysine acetylation. Disruption of this balance fundamentally alters CBP's chromatin occupancy, patterns of histone acetylation, and downstream gene expression. Together, our work reveals an unexpected mechanism of intramolecular cooperation between distinct IDRs and highlights how their properties shape the functional landscape of multi-domain proteins.

INTRODUCTION

Intrinsically disordered regions (IDRs) are protein sequences that lack stable secondary or tertiary structures yet serve as vital regulators of biological function.[1,2] By leveraging compositional biases and specific amino acid patterning, IDRs mediate multivalent interactions that shape the formation and physical behavior of biomolecular condensates.[1,3] Because they adopt a vast conformational ensemble, IDRs are uniquely responsive to their environmental context[4,5]; however, while the rules governing individual disordered segments are becoming clearer, it remains poorly understood how multiple, distinct IDRs within a single protein integrate their properties to generate specific biological functions. An example of this problem is found in *cAMP response element-binding protein* (CREB)-*binding protein* (CBP) and its paralog *EP300* (p300), essential histone acetyltransferases (HATs). By combining a structured catalytic domain with large IDRs, CBP and p300 integrate HAT activity with the conformational plasticity needed to interact with diverse transcription factors (TFs) at *cis*-regulatory elements (CREs).

CBP and p300 control the strength of transcription by mediating lysine acetylation on histones and TFs while simultaneously facilitating RNA polymerase II recruitment and the maintenance of promoter-proximal pausing[6–10] and forming biomolecular condensates that regulate transcriptional bursting.[11] IDRs and condensates are central to many of CBP's functions. For example, TF binding is frequently mediated by IDRs that undergo "coupled folding and binding" with TFs,[12–14] while HAT activity is regulated by the disordered autoregulatory loop (CBP_{AL}), which typically blocks the active site but is displaced by autoacetylation or binding to non-coding enhancer RNAs (eRNAs) to stimulate catalysis.[15–18] Interestingly, the relationship between phase behavior and activity appears context dependent: while molecular

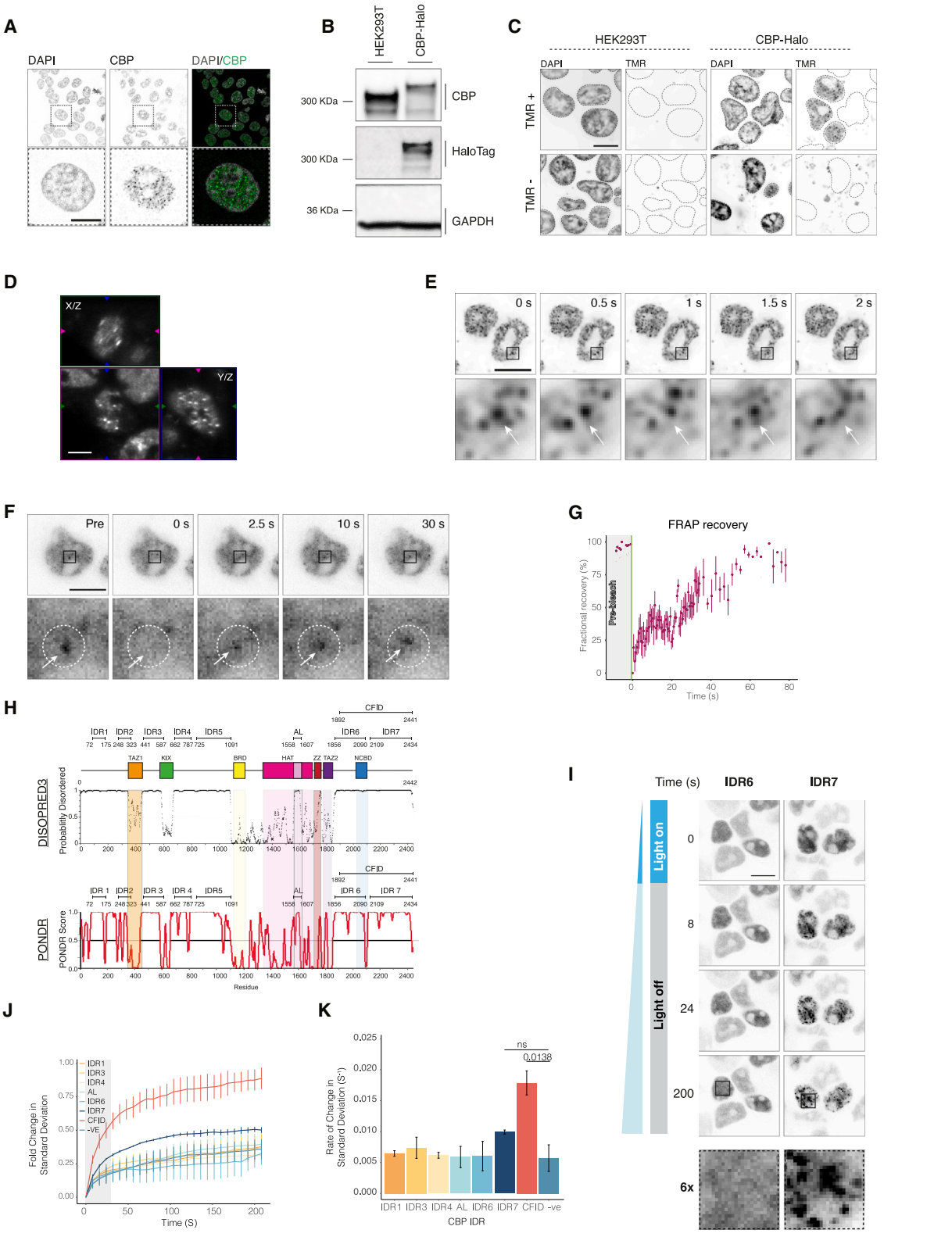

Figure 1. CBP forms fluid-like puncta in the nucleus

(A) Immunofluorescence of CBP in HEK293T cells; scale bars, 10 μm.

(B–D) CBP-Halo HEK293T cells: (B) western blot, (C) confocal microscopy of CBP-Halo$_{TMR}$, (D) lattice light-sheet microscopy. Scale bars, 10 μm (C) and 5 μm (D).

(legend continued on next page)

crowding and condensates can inhibit p300 HAT-domain activity *in vitro,*[19,20] TF binding outside the HAT domain can regulate HAT activity,[21] and TF-driven condensation in cells correlates with increased genome-wide acetylation.[11]

This sensitivity to the physical environment suggests that CBP function relies on a complex intramolecular balance between its various disordered regions. To decipher this complexity, we systematically characterized the impact of distinct CBP-IDRs on CBP's cellular behavior and found that they play remarkably different roles. Specifically, we demonstrate that two adjacent C-terminal IDRs, despite different amino acid compositions and patterning, work in tandem to regulate how CBP responds to environmental cues such as acetylation. Disruption of these regions fundamentally alters CBP condensate dynamics, chromatin localization, and transcriptional output. Our results uncover unexpected functional roles for these sequences and highlight how intramolecular cooperation between distinct CBP-IDRs shapes the behavior of multi-domain coactivators.

RESULTS

CBP forms fluid-like condensates in the nucleus

To validate the formation of CBP condensates, we imaged endogenous CBP by immunofluorescence (IF) in HEK293T cells, revealing distinct nuclear puncta consistent with previous observations[22,23] (Figure 1A). To uncover the behavior of these puncta, we introduced an in-frame HaloTag to the C terminus of endogenous CBP (CBP-Halo; Figures 1B and S1A–S1C). Live-cell imaging using the fluorescent Halo ligand TMR (CBP-Halo$_{TMR}$) showed that CBP-Halo formed endogenous puncta (Figure 1C). Using lattice light-sheet microscopy, we visualized the spatial organization of CBP puncta (Figure 1D). CBP-Halo formed, on average, 27.9 condensates/nucleus, with a mean volume of 33 ± 14.6 μm^3 and an integrated intensity density (IID) of 835.6 ± 132.8. Importantly, CBP-Halo$_{TMR}$ condensates exhibited fluid behavior, fusing and dispersing within the 2-s imaging window (Figure 1E; Video S1). We next tested fluid-like behavior using fluorescence recovery after photo bleaching (FRAP) on endogenous CBP labeled with Janelia Fluor 549 (CBP-Halo$_{JF549}$). CBP-Halo$_{JF549}$ recovered to ∼50% of its pre-bleach levels after 30 s and to ∼90% after 60 s (Figures 1F and 1G; Video S2). These data clearly establish fluid-like behavior of endogenous CBP-Halo condensates.

IDRs in CBP have distinct abilities to form condensates

Wild-type (WT) CBP (CBP$_{WT}$) is predicted to be ∼65% disordered (Figure 1H), and AlphaFold2[26] shows interspersed structured domains and IDRs (Figure S1D). We identified nine IDRs for further analysis, using a threshold of 50 consecutive amino acids with a predicted disorder >50% (CBP$_{IDR1\text{-}IDR7}$; Figure 1H) in PONDR[25] to define IDR boundaries. We also tested the CBP:FUS interaction domain (CBP$_{CFID}$), which binds to fused-in-sarcoma (FUS),[27] which contains CBP$_{IDR6}$ and CBP$_{IDR7}$ and CBP$_{AL}$. The behavior of IDRs is governed by non-random amino acid compositions and non-random patterning of amino acids. To uncover compositional and sequence biases in CBP-IDRs, we used NARDINI+, which compares the enrichment and depletion of sequence features to their distribution across all human IDR-containing proteins,[28,29] revealing enrichment or depletion of sequence features in CBP-IDRs (Figure S1E). For example, CBP$_{IDR7}$ was enriched for glutamine residues and glutamine patches and depleted for hydrophobic residue pairs, while CBP$_{AL}$ was enriched for asparagine, lysine patches, and positive/negative residue pairs. In contrast, CBP$_{IDR4}$ and CBP$_{IDR6}$ had an elevated ratio of arginine and lysine residues, a higher fraction of proline residues, and a higher propensity to adopt polyproline II conformations,[30] consistent with previous NMR studies.[31]

We next tested whether CBP-IDRs could form condensates through homotypic interactions using the OptoDroplet system.[32] Candidate IDRs were fused to the photoactivatable photolyase homology region of Cry2 (Cry2PHR) and an SV40 nuclear localization sequence (NLS; Figure S1F). Upon blue light exposure, condensing IDRs (e.g., CBP$_{IDR7}$) formed puncta, whereas non-condensing IDRs (e.g., CBP$_{IDR6}$) did not (Figures 1I and S1G). To quantify condensation, we measured the standard deviation (SD) of nuclear intensity. While most CBP-IDRs mirrored the negative control, CBP$_{IDR7}$ and CBP$_{CFID}$ showed rapid SD increases following photoactivation, indicating robust condensate formation (Figures 1J and S1H). Initial rates of droplet formation (0–30 s after blue light) confirmed that only CBP$_{IDR7}$ and CBP$_{CFID}$ formed more condensates than Opto-NLS controls (Figures 1K and S1I). Together, these results demonstrate distinct phase behavior across CBP-IDRs, identifying the C-terminal domain as a primary driver of condensation.

CBP-IDRs regulate the number of CBP condensates

We next tested how CBP-IDRs contribute to CBP$_{WT}$ condensates. CBP-IDRs were deleted in CBP$_{WT}$ fused to an in-frame C-terminal GFP tag (CBP$_{WT}$-GFP; Figure 2A). For CBP$_{\Delta AL}$-GFP, we used a flexible linker to maintain correct folding.[33] CBP-GFP constructs showed similar expression (Figure S2A), although we cannot rule out the possibility of variable cell-to-cell transfection within each population.

To quantify puncta, cells were fixed and imaged by confocal microscopy (Figures 2B and S2B). Data were initially selected for successful transfection and then blind-scored for punctate

(E) Dynamic behavior of CBP-Halo$_{TMR}$ condensates (see also Video S1). Boxes indicate enlarged regions. Scale bar, 10 μm.
(F and G) FRAP of CBP-Halo$_{JF549}$ condensates. (F) Confocal microscopy showing FRAP; scale bar, 10 μm. (G) FRAP curves; n = 7 (see also Video S1).
(H) CBP$_{WT}$ domain map and predicted disorder. DISOPRED3[24] (top); PONDR[25] (bottom).
(I and J) (I) OptoDroplet of CBP$_{IDR6}$ and CBP$_{IDR7}$. Boxes indicate enlarged regions. Scale bar, 10 μm. (J) Fold change in SD of gray values. Shading highlights initial 30 s. Bars represent mean ± SEM; n = 3 biological replicates.
(K) Initial rate of change calculated over initial 30 s. AL, autoregulatory loop; -ve, Opto-NLS negative control. Bars represent mean ± SEM (ns, not significant); n = 3 biological replicates, p values from unpaired t test.
See also Figure S1.

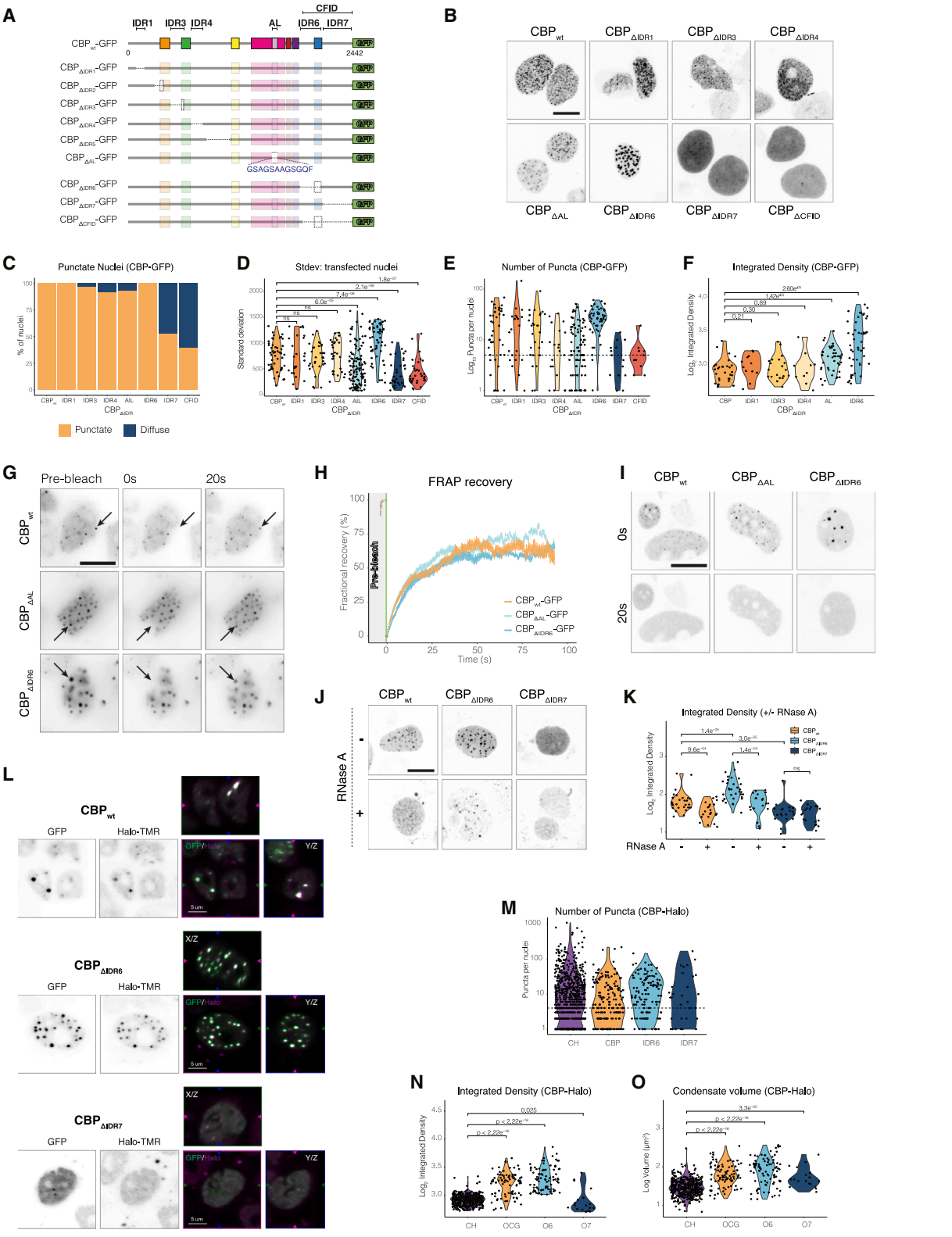

(legend on next page)

or diffuse nuclear signal (Figures 2C and S2C). Most constructs, including CBP_{WT}-GFP, $CBP_{\Delta IDR1}$-GFP, and $CBP_{\Delta IDR6}$-GFP, showed high puncta formation (>91%). In contrast, $CBP_{\Delta IDR7}$-GFP and $CBP_{\Delta CFID}$-GFP were less punctate (52.9% and 40.0%, respectively). Quantitative analysis of nuclear intensity SD (Figure 2D) supported these trends, identifying $CBP_{\Delta IDR6}$-GFP as significantly enriched for condensates, while $CBP_{\Delta AL}$-GFP, $CBP_{\Delta IDR7}$-GFP, and $CBP_{\Delta CFID}$-GFP were significantly depleted. Although informative, these categorical descriptions were insufficient to resolve the full complexity of CBP phase behavior.

We therefore applied an unbiased filter for noise and artifacts (Figures S2E–S2G), then calculated mean condensate numbers per nucleus (Figures 2E and S2H). CBP_{WT}-GFP and most CBP-IDR deletions formed >6 condensates per nucleus in >80% of cells (Figures 2B–2E, S2B, and S2H). While $CBP_{\Delta IDR1}$-GFP and $CBP_{\Delta IDR3}$-GFP mirrored CBP_{WT}-GFP, behavior, $CBP_{\Delta IDR4}$-GFP and $CBP_{\Delta AL}$-GFP reduced condensate frequency by ~50% (Figure 2E). Condensate numbers per nucleus were highly variable (Figure S2I). CBP_{WT}-GFP had an SD-to-mean ratio of 0.86, with most CBP-IDR deletions showing similarly high ratios ranging from 0.75 ($CBP_{\Delta IDR7}$-GFP) to 1.37 ($CBP_{\Delta IDR1}$-GFP).

Unlike other variants, $CBP_{\Delta CFID}$-GFP and $CBP_{\Delta IDR7}$-GFP remained largely diffuse (60% and 47%, respectively; Figure 2C). These mutants exhibited significantly reduced intensity SD and an ~75% decrease in puncta frequency compared to WT (Figures 2D, 2E, and S2I). Visual inspection confirmed that residual puncta in these cells were poorly defined (Figure 2B). Coupled with OptoDroplet results (Figures 1I–1K), these data identify the C-terminal IDRs as essential drivers of CBP condensation.

Intriguingly, $CBP_{\Delta IDR6}$-GFP exhibited significantly higher intensity SD and ~30% more condensates than CBP_{WT}-GFP (Figure 2D). These condensates were more uniform in number (SD ratio = 0.49; Figure S2I), suggesting that CBP_{IDR6} normally promotes variability. Notably, while the larger CBP_{CFID} region is essential for phase separation, these results reveal that the C terminus contains modules with opposing abilities to both promote and inhibit condensation.

CBP-IDRs regulate the size and intensity of CBP condensates

Deletion of CBP-IDRs clearly altered the morphology of CBP condensates (Figure 2B). To quantify this behavior, we measured the IID, excluding the mostly diffuse $CBP_{\Delta CFID}$-GFP and $CBP_{\Delta IDR7}$-GFP. While the IID of most CBP-IDR deletions mirrored CBP_{WT}-GFP condensates (870 ± 72 SEM), $CBP_{\Delta AL}$-GFP and $CBP_{\Delta IDR6}$-GFP showed 1.5-fold and 3-fold increases, respectively (Figures 2F and S2J). This suggests that AL and IDR6 normally restrict CBP condensate size and intensity. FRAP confirmed that CBP_{WT}-GFP, $CBP_{\Delta AL}$-GFP, and $CBP_{\Delta IDR6}$-GFP condensates remained fluid. All variants recovered rapidly (rates: 0.11–0.13 s^{-1}; Figures 2G, 2H, and S2K), with only subtle differences in mobility, consistent with liquid-like properties. Application of 5% 1,6-hexanediol (1,6-HD), which disrupts weak hydrophobic interactions, dissolved CBP_{WT}-GFP, $CBP_{\Delta IDR6}$-GFP, and $CBP_{\Delta AL}$-GFP condensates in <20 s (Figure 2I). This indicated that hydrophobic interactions are important for maintaining CBP condensates. Since CBP binds RNA, we tested how RNase A treatment affects condensate stability (Figure 2I). Treating cells with 0.5 μM RNase A decreased the proportion of punctate nuclei, size, and intensity of CBP_{WT}-GFP and $CBP_{\Delta IDR6}$-GFP condensates, while $CBP_{\Delta IDR7}$-GFP remained largely unaffected (Figure S2L). Interestingly, condensate numbers increased across all constructs, likely due to puncta dispersal following RNA degradation (Figure S2M). These results suggest that cellular RNAs help maintain CBP condensates.

These findings reveal how CBP-IDRs exert distinct regulatory control over CBP condensates. CBP_{IDR7} is a dominant driver of condensation but is balanced by CBP_{IDR6} and CBP_{AL}, which constrain condensate size and intensity. Furthermore, CBP condensates appear to be supported by hydrophobic interactions and stabilized by RNA, highlighting a complex balance that tunes condensate properties.

CBP IDRs regulate endogenous CBP condensates

Both endogenous CBP-Halo and CBP-GFP form fluid-like condensates (Figures 1E–1G, 2F, and 2G). These assemblies typically arise from a combination of homotypic IDR self-association and heterotypic interactions with RNAs or other proteins.[34] We hypothesized that our observed phenotypic changes stem, at least in part, from altered homotypic IDR interactions. To test this, we investigated whether deleting specific CBP-IDRs could regulate endogenous CBP condensate behavior.

Using lattice light-sheet microscopy, we imaged endogenous CBP-Halo (JF646-labeled, $CBP\text{-}Halo_{JF646}$) alongside GFP-tagged CBP-IDR mutants (Figure 2L). Compared to controls,

Figure 2. CBP-IDRs affect the behavior of full-length CBP_{WT}

(A) $CBP_{\Delta IDR}$-GFP constructs.

(B–F) Confocal microscopy of CBP-GFP condensates in HEK293T. (B) Maximum projection; scale bar, 10 μm. (C) Percentage of nuclei displaying diffuse or punctate signal. (D) SD of gray values. (E) Number of condensates per nucleus. Dashed line shows 6 puncta per nucleus threshold. (F) Integrated intensity density (IID). n = 3 biological replicates; p values by Kruskal-Wallis test.

(G and H) FRAP of CBP_{WT}-GFP, $CBP_{\Delta IDR6}$-GFP, and $CBP_{\Delta AL}$-GFP. (G) Confocal microscopy showing FRAP; scale bar, 10 μm. (H) FRAP curves. Relative fluorescence recovery normalized to pre-bleached intensity for a 90 s time period following bleaching. Gray shading highlights imaging pre-bleach; green line denotes bleaching. Still images from Videos S6, S7, and S8.

(I) 1,6-hexanediol treatment; scale bar, 10 μm. See also Videos S3, S4, and S5.

(J and K) RNase treatment. (J) Cells were treated with 100 μg/mL RNase A for 20 min; images were taken pre- and post-treatment; scale bars, 5 μm. (K) IID.

(L–O) CBP_{WT}-GFP, $CBP_{\Delta IDR6}$-GFP, and $CBP_{\Delta IDR7}$-GFP showing dominant phase separation phenotype on $CBP\text{-}Halo_{JF646}$ condensates. (L) Lattice light-sheet microscopy; scale bars, 5 μm. (M) Number of condensates per nucleus. Dashed line represents a threshold value of 6 puncta per nuclei. (N) IID. (O) Condensate volume (μm^3). Data points highlight individual nuclei. n = 3 biological replicates; p values by Kruskal-Wallis test.

See also Figure S2.

CBP_{WT}-GFP slightly reduced the number of endogenous condensates while increasing their IID (Figures 2M and 2N) and volume (Figure 2O), likely due to co-expressed CBP molecules. Notably, relative to CBP_{WT}-GFP, $CBP_{\Delta IDR6}$-GFP further increased endogenous condensate IID and volume, whereas $CBP_{\Delta IDR7}$-GFP exerted the opposite effect (Figures 2N and 2O). These trends were confirmed with live-cell confocal microscopy (Figure S2N) without channel bleed-through (Figure S2O).

Although we cannot rule out complexities arising from mixed populations of endogenous and exogenous CBP, these data underscore the importance of homotypic CBP-IDR interactions, with CBP_{IDR6} and CBP_{IDR7} acting as dominant-positive and -negative regulators, respectively. Although heterotypic interactions likely also occur (as reported for p300),[11] the ability of IDRs to drive condensation homotypically suggests that IDR modifications or disease mutations could broadly tune CBP activity by altering its condensate landscape.

Opposing properties of CBP-IDRs reflect their sequence characteristics

To determine if the opposing behaviors of CBP_{IDR6} and CBP_{IDR7} are sequence encoded, we analyzed their properties using localCIDER[35] (Figure 3A). Relative to CBP_{WT}, the C-terminal CBP_{CFID} is enriched for prolines and polar residues, favoring expanded conformations,[36] but depleted of charged and aromatic amino acids. Individually, CBP_{IDR7} is more polar than CBP_{IDR6} (54% vs. 41%), while CBP_{IDR6} is more proline rich than CBP_{IDR7} (21% vs. 14%). Notably, CBP_{IDR7} displays a biased linear distribution (Figure 3B), with polar residues clustered around an 18-residue polyQ tract and proline concentrated toward the C terminus.

To isolate the role of sequence patterning, we used GOOSE[38] to design compositionally identical but randomly shuffled mutants of CBP_{IDR6} and CBP_{IDR7} (Figures S3A and S3B). NARDINI+ analysis confirmed that while global composition, including the fraction of glutamine (FracQ) and charged residues (FCRs), remained constant, pairwise patterning was significantly altered (Figure 3C, bold). Notably, CBP_{IDR6} is enriched for leucine patches and hydrophobic-proline pairs, features lost upon shuffling. Conversely, CBP_{IDR7} is depleted of hydrophobic and polar-proline pairs, which were enriched upon shuffling (Figure 3C).

To determine if sequence patterning is important for condensate behavior, we expressed shuffled CBP-IDR mutants and imaged them using confocal microscopy (Figure 3D). Following filtering (Figure S3D), $CBP_{IDR6\text{-}Shuffle}$-GFP mirrored the $CBP_{\Delta IDR6}$-GFP phenotype, forming additional, larger, and more uniform condensates than CBP_{WT}-GFP (Figures 3E, 3F, and S3E). This suggests that the order and sequence patterning of amino acids in CBP_{IDR6} is essential for its regulatory function. Conversely, $CBP_{IDR7\text{-}Shuffle}$-GFP maintained CBP_{WT}-like condensates, contrasting with the diffuse signal of $CBP_{\Delta IDR7}$-GFP. The result suggests that CBP_{IDR7}'s ability to drive condensation depends primarily on its global composition, including its glutamine enrichment and the ratio of arginine and lysine residues (Figure 3C, bold), rather than specific pairwise patterning.

Given their polar and polyQ enrichment (Figure 3C), which are associated with the prion-like domain (PrLD),[39] we investigated whether CBP_{IDR6} and CBP_{IDR7} could exhibit prion-like behavior using prion-like amino acid composition (PLAAC) analysis (Figure 3C).[37] PLAAC identified a large, contiguous PrLD in CBP_{IDR7} (Figure 3F), which expanded in $CBP_{IDR7\text{-}Shuffle}$. This PrLD aligns with CBP_{IDR7}'s necessity for condensate formation (Figures 2B–2E) and its self-association in OptoDroplet assays (Figures 1I–1K). CBP_{IDR6} was also predicted to contain PrLDs, but these were discontiguous and smaller than in CBP_{IDR7}, potentially explaining its distinct behavior.

Finally, we asked if the distinct properties of CBP_{IDR6} and CBP_{IDR7} are conserved in its paralog, p300. While the HAT domains are 87% identical, the IDRs are significantly more divergent (48%–56% identity; Figure S3J). NARDINI+ analysis revealed that $p300_{IDR7}$ possesses a distinct charge and patterning profile compared to CBP_{IDR7}, including a higher Arg:Lys ratio (Figure S3K). Furthermore, while PLAAC confirmed a large, contiguous PrLD in $p300_{IDR7}$, it also predicted a contiguous PrLD in $p300_{IDR6}$, contrasting with the fragmented prion-like regions of CBP_{IDR6}. Taken together, these sequence-level differences suggest that p300 and CBP condensates may behave differently.

CBP-IDRs allow global lysine acetylation to shape CBP condensates

Our results show that distinct sequence properties within CBP-IDRs cause different properties in CBP condensates. We hypothesize that this influences how other environmental inputs, such as post-translational modifications (PTMs), regulate CBP function. CBP and p300 acetylate nearly one-third of nuclear proteins, including themselves,[8] and lysine acetylation plays a complex role in regulating CBP/p300 function.[11,17,20,40] However, it remains unknown how these regulatory events combine with CBP-IDR-mediated regulation of condensates.

To test how CBP-IDRs respond to global lysine acetylation, we used HAT inhibitor A-485[41] to deplete CBP- and p300-dependent acetylation and monitored the resulting behavior of $CBP_{\Delta IDR6}$-GFP and $CBP_{\Delta IDR7}$-GFP condensates (Figure 4A). Treating cells with 5 μM A-485 for 36 h[41] highlighted sensitivity to acetylation due to CBP-IDRs: while A-485 increased the proportion of punctate nuclei in CBP_{WT}-GFP without affecting condensate intensity (Figures 4B–4D), it significantly reduced the size and intensity of $CBP_{\Delta IDR6}$-GFP condensates (Figure 4D). Conversely, while A-485 increased the proportion of cells with $CBP_{\Delta IDR7}$-GFP puncta, their size and intensity remained lower than controls (Figures 4B–4D). These results suggest that deleting CBP_{IDR6} increases condensate sensitivity to global acetylation, whereas acetylation cannot overcome deficiencies due to CBP_{IDR7} deletion.

We next tested the response of condensates to hyperacetylation and chromatin de-compaction by treating cells with 500 nM trichostatin A (TSA), a general inhibitor of histone deacetylases (HDACs), for 90 min.[42] Treatment slightly increased the proportion of punctate nuclei in CBP_{WT}-GFP and $CBP_{\Delta IDR7}$-GFP cells (Figure 4B) but did not affect the number and IID of condensates. In contrast, both the number of $CBP_{\Delta IDR6}$-GFP condensates and their IID increased following application of TSA (Figures 4B–4D). The result highlights that deleting CBP_{IDR6} increases condensate sensitivity to global acetylation.

CellPress
OPEN ACCESS

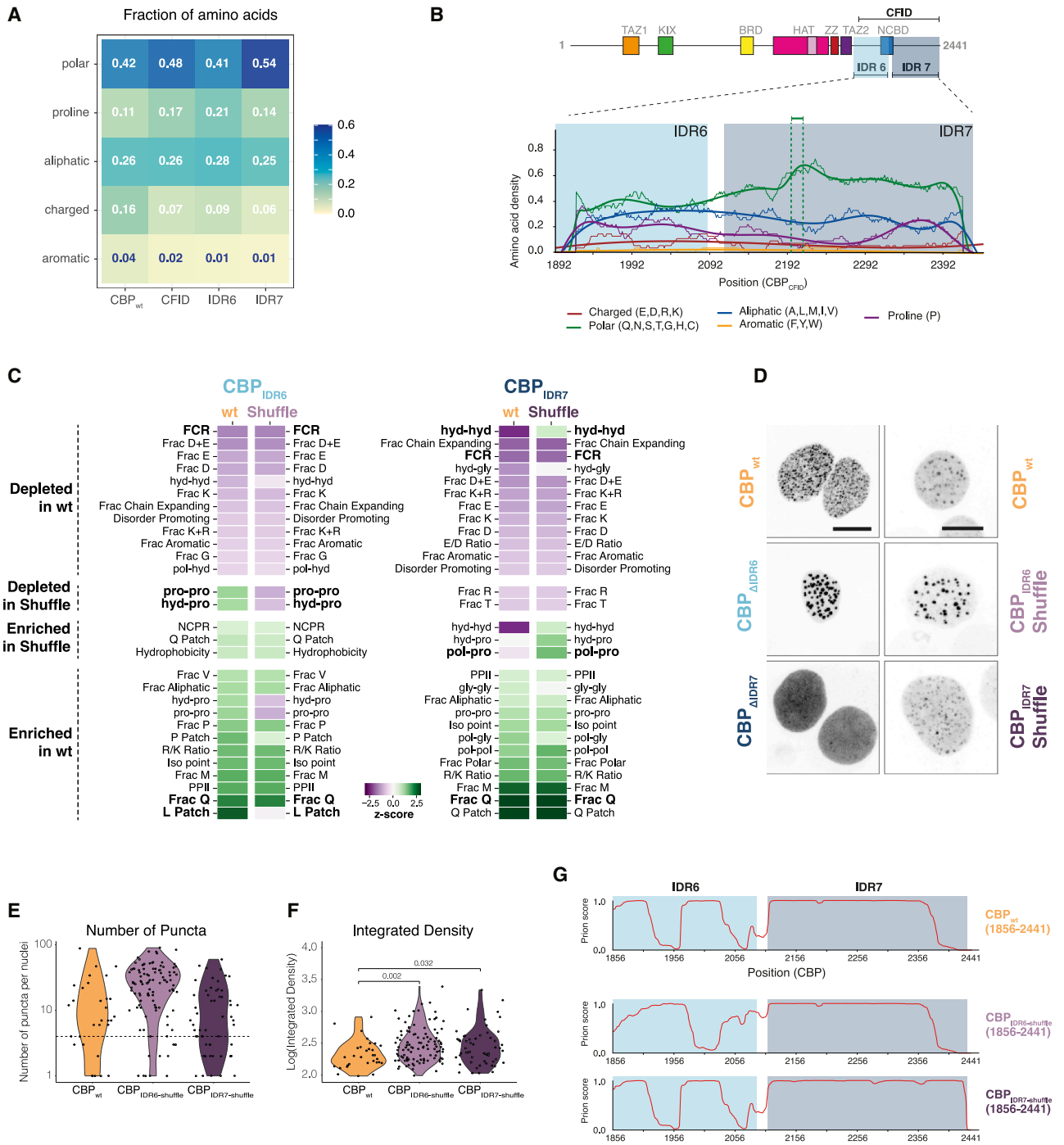

Figure 3. Sequence properties of CBP-IDRs

(A) Sequence properties of CBP_{WT}, CBP_{CFID}, CBP_{IDR6}, and CBP_{IDR7}. Amino acids are grouped by property: polar (Q, N, S, T, G, H, C); proline (P); aliphatic (A, L, M, I, V); charged (E, D, R, K); aromatic (F, Y, W).[35] Numbers indicate the fraction of amino acids with each property.

(B) Linear amino acid composition[35]; green bar highlights 18× polyQ.

(C) Comparison of the 12 most-enriched or -depleted sequence parameters (relative to all human IDR proteins) in CBP_{WT} and shuffle mutants, using NARDINI+.[28,29] Features from main text are highlighted in bold.

(D–F) Effect of shuffled IDRs on CBP condensates. (D) Confocal microscopy; scale bars, 10 μm. (E) Number of condensates per nucleus. (F) IID; $n = 3$ biological replicates. p values by Kruskal-Wallis test.

(G) PLAAC analysis[37] showing CBP_{WT}, $CBP_{IDR6\text{-}shuffle}$, and $CBP_{IDR7\text{-}shuffle}$.

See also Figure S3.

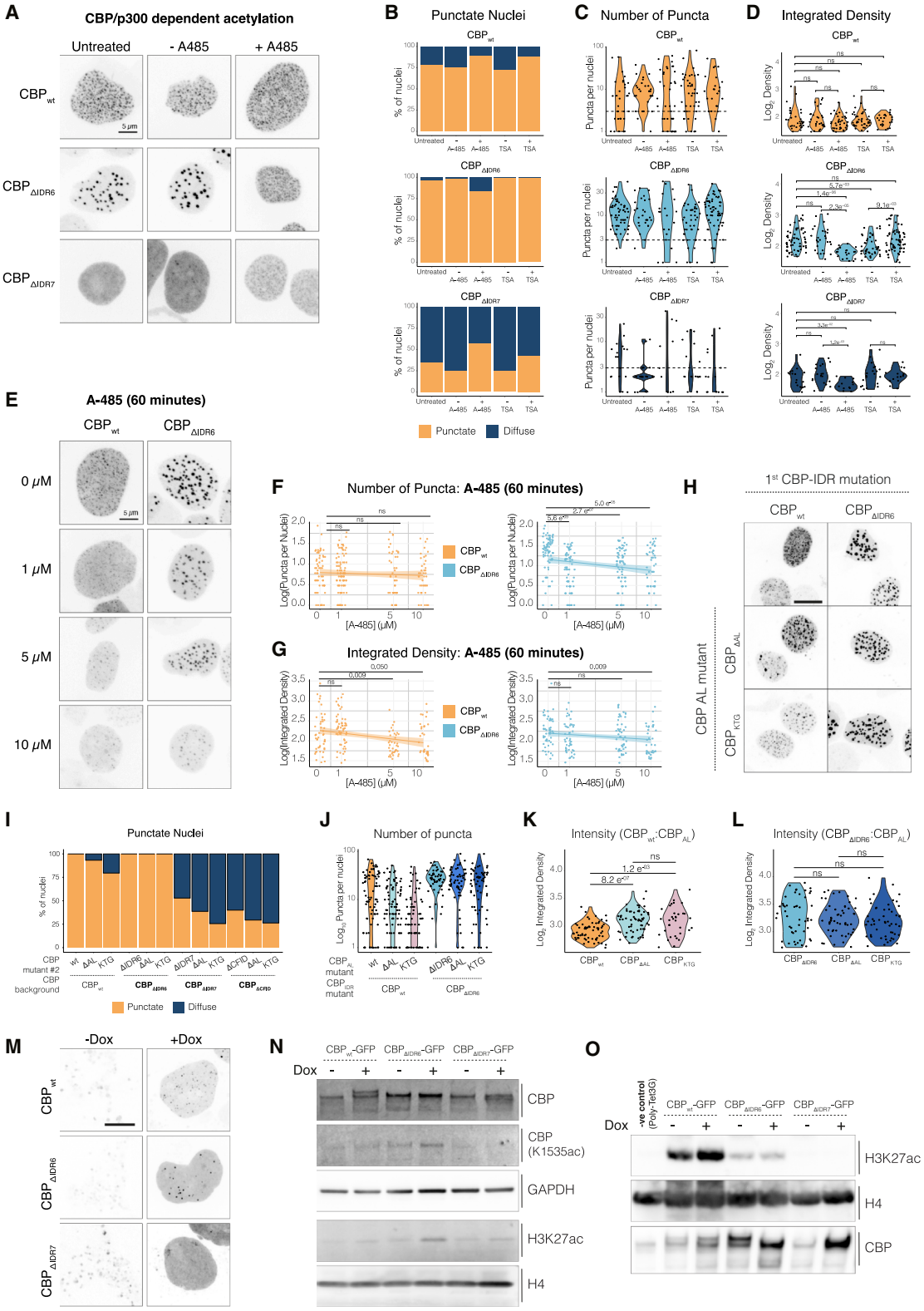

(legend on next page)

Unexpectedly, our CBP_{WT}-GFP data diverged from reported p300 results, where higher A-485 concentrations increased puncta number but decreased size.[11] To investigate, we tested varying A-485 concentrations (up to 10 μM) and shorter durations (0–120 min; Figures 4E and S4C). Unlike p300, CBP_{WT}-GFP puncta number remained stable across all conditions (Figures 4F and S4D), with intensity decreasing significantly only at 10 μM after 120 min (Figures 4G and S4E). Conversely, $CBP_{\Delta IDR6}$-GFP showed heightened sensitivity, with A-485 causing a pronounced drop in condensate number (Figures 4E and S4D); while 10 μM A-485 modestly decreased $CBP_{\Delta IDR6}$-GFP intensity at 60 min, this effect was not sustained at 120 min (Figures 4G and S4E).

Experiments with A-485 and TSA reveal the potential importance of CBP_{IDR6} for buffering CBP's response to global acetylation: its removal makes CBP condensates hypersensitive to changes in acetylation. However, A-485 and TSA affect global levels of acetylation, which makes it challenging to separate changes in condensates due to direct acetylation of CBP from indirect disruption of heterotypic interactions.

Regulation of condensates by acetylation of CBP_{AL} relies on CBP-IDR integrity

To assess how direct acetylation of CBP_{AL} regulates condensation, we compared $CBP_{\Delta AL}$-GFP and CBP_{KTG}-GFP (a non-acetylatable lysine-to-glycine mutant) (Figures 2A and S4F). Both mutations reduced the proportion of punctate nuclei and decreased condensate frequency by 40%–60% relative to CBP_{WT}-GFP (Figures 4H–4J). However, both mutants showed a 40%–50% increase in condensate size and intensity (Figure 4K). These results mirror previous *in vitro* findings for p300,[20] suggesting that while the CBP_{AL} sequence promotes condensate nucleation, lysine acetylation within the CBP_{AL} serves to limit their growth.

To determine how CBP-IDRs and CBP_{AL} acetylation intersect, we generated double mutants combining $CBP_{\Delta IDR6}$-GFP or $CBP_{\Delta IDR7}$-GFP with the AL mutations ($CBP_{\Delta AL}$ and CBP_{KTG}). Because $CBP_{\Delta IDR7}$-GFP and $CBP_{\Delta CFID}$-GFP fail to form condensates, they were unaffected by CBP_{AL} mutations (Figures S4G–S4I). Notably, the CBP_{AL} mutations, which significantly altered CBP_{WT}-GFP behavior, had no effect on the proportion, number, or intensity of $CBP_{\Delta IDR6}$-GFP condensates (Figures 4I–4L). This suggests that CBP_{IDR6} is essential for CBP_{AL} acetylation to regulate condensate behavior; without CBP_{IDR6}, the regulatory influence of CBP_{AL} is lost.

To compare direct CBP_{AL} acetylation with global acetylation, we treated cells expressing $CBP_{WT/KTG}$-GFP or $CBP_{\Delta IDR6/KTG}$-GFP with A-485. Similar to the single mutants, A-485 treatment slightly reduced condensate size and intensity in $CBP_{WT/KTG}$-GFP but caused a more pronounced decrease in $CBP_{\Delta IDR6/KTG}$-GFP (Figure S4J). Because these mutants cannot be acetylated at the CBP_{AL}, these findings emphasize that global acetylation promotes condensation and further demonstrate that CBP_{IDR6} deletion hypersensitizes condensates to global acetylation levels.

Together, these findings reveal a complex regulatory landscape for CBP condensates. While global acetylation minimally impacts CBP_{WT}, direct CBP_{AL} acetylation appears to promote more frequent, smaller condensates. CBP-IDRs remain dominant regulators: CBP_{IDR7} is essential for condensate formation, whereas CBP_{IDR6} deletion consistently yields more and larger puncta, regardless of CBP_{AL} status. This suggests that CBP_{IDR6} is required for CBP_{AL}-mediated regulation. However, the CBP_{AL} mutant data require cautious interpretation: given the region's functional importance, mutations may have pleiotropic effects; CBP_{AL} deletion can increase catalytic activity,[17] potentially driving condensation via histone acetylation,[40] while lysine mutations may disrupt RNA binding,[15] a known driver of condensate behavior independent of acetylation.[43]

IDRs regulate CBP-dependent acetylation

To assess if CBP-IDRs affect histone acetylation, we generated doxycycline-inducible HEK293T clonal lines for CBP_{WT}-GFP, $CBP_{\Delta IDR6}$-GFP, and CBP_{IDR7}-GFP. We used doxycycline concentrations that maintained near-endogenous CBP-GFP levels (Figures S4K and S4L). Consistent with our transient expression data, CBP_{WT}-GFP and $CBP_{\Delta IDR6}$-GFP formed condensates, although condensate numbers were smaller, while CBP_{IDR7}-GFP remained diffuse (Figures 4M, S4M, and S4N). Notably, $CBP_{\Delta IDR6}$-GFP condensates were significantly larger and more intense (mean IID = 126.0 ± 21.5) than CBP_{WT}-GFP (mean IID = 80.6 ± 18.3), whereas $CBP_{\Delta IDR7}$-GFP failed to form quantifiable puncta (Figure S4O).

To assess the impact of CBP-IDRs on histone acetylation, we measured H3K27ac levels in our inducible lines. In cells, $CBP_{\Delta IDR6}$-GFP caused a >2-fold increase in global H3K27ac, whereas CBP_{IDR7}-GFP slightly decreased H3K27ac (Figures 4N and S4P). While activated CBP (K1535ac) levels remained stable for CBP_{WT}-GFP and $CBP_{\Delta IDR6}$-GFP, they were depleted

Figure 4. CBP-IDRs affect response to acetylation

(A) Confocal microscopy after 48-h treatment with 0.5 μM A-485; scale bar, 5 μm.

(B–D) Effect of A-485 and TSA on CBP condensates. (B) Percentage of nuclei displaying diffuse or punctate signal; (C) Number of condensates per nucleus. (D) IID. Cells were treated with A-485 for 36 h[41] and with TSA for 90 min.[42] n = 3 biological replicates; p values by Kruskal-Wallis test.

(E–G) A-485 concentrations affect CBP condensates. (E) Confocal microscopy after 60 min with A-485 (0 μM = DMSO); scale bar, 5 μm. (F) Number of condensates per nucleus. (G) IID; scale, pseudo-log base 10. n = 3 biological replicates; p values by Kruskal-Wallis test.

(H–L) CBP_{AL} acetylation. (H) Confocal microscopy; scale bar, 10 μm. (I) Percentage of nuclei displaying diffuse or punctate signal. (J) number of condensates per nucleus. (K) IID (CBP_{WT}-GFP background). (L) IID ($CBP_{\Delta IDR6}$-GFP background). n = 3 biological replicates; p values by Kruskal-Wallis test.

(M) Inducible CBP-GFP expression. Confocal microscopy of CBP-GFP HEK293T cells treated with doxycycline (Dox) for 48 h. Dox concentrations: CBP_{WT}-GFP, 25 ng/mL^{-1}; $CBP_{\Delta IDR6}$-GFP, 5 ng/mL^{-1}; CBP_{IDR7}-GFP, 25 ng/mL^{-1}; scale bar, 10 μm.

(N) Acetylation following Dox induction of CBP-GFP. CBP was resolved using 3%–8% Tris-acetate PAGE (loading control: GAPDH). H3K27ac was resolved using 12% Bis-Tris PAGE (loading control: histone H4).

(O) Immunoprecipitation HAT assay using recombinant di-nucleosomes.

See also Figure S4.

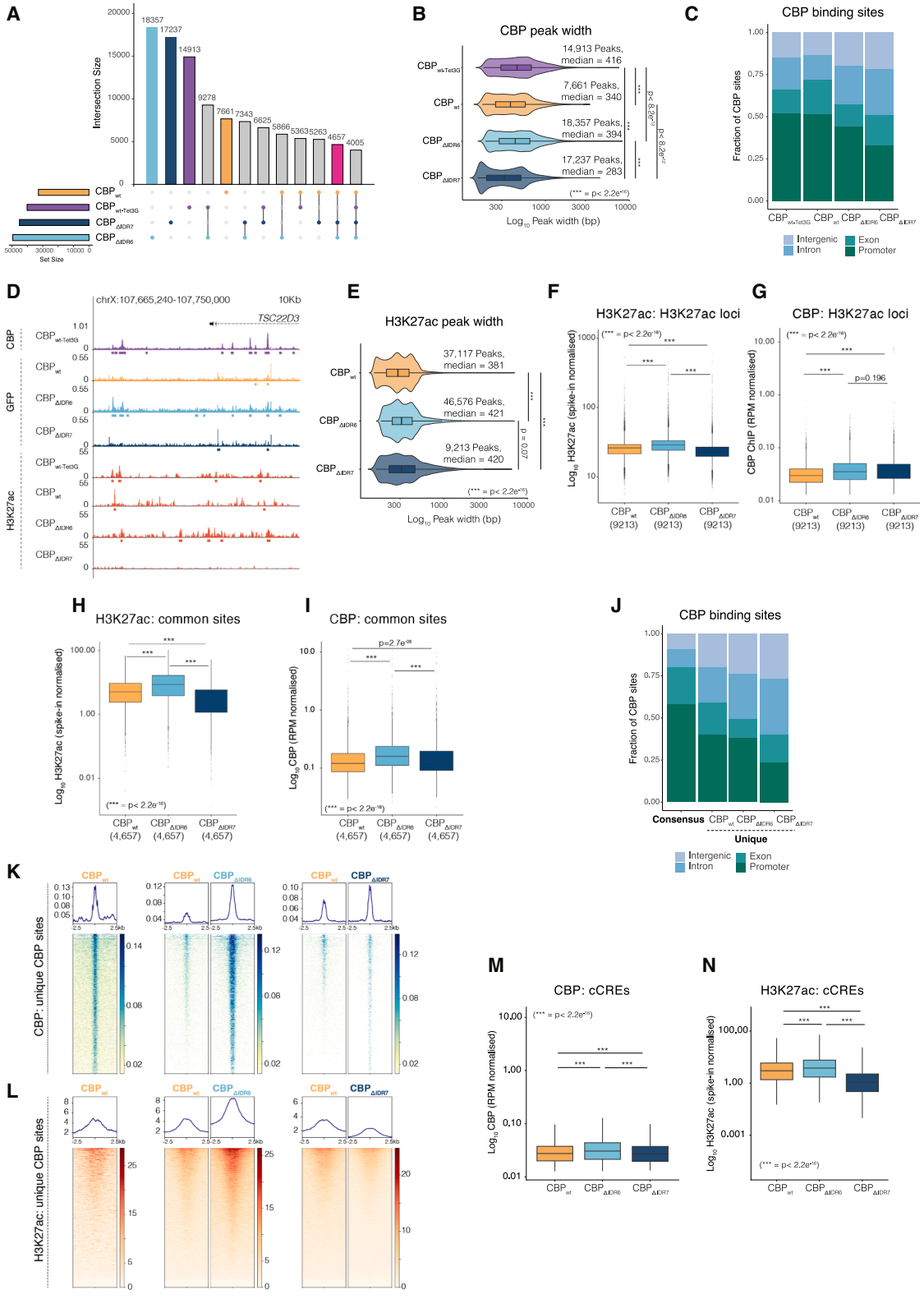

Figure 5. CBP-IDRs regulate nuclear chromatin association and H3K27ac

(A) Overlap between CBP binding sites. $CBP_{WT\text{-}Tet3G}$ (purple), CBP_{WT}-GFP (orange), $CBP_{\Delta IDR6}$-GFP (light blue), and CBP_{IDR7}-GFP (dark blue). Magenta bar highlights sites common between each dataset.

(legend continued on next page)

in the $CBP_{\Delta IDR7}$-GFP mutant (Figures 4N and S4Q). Surprisingly, *in vitro* HAT assays using immunoprecipitated proteins and recombinant nucleosomes showed the opposite trend: CBP_{WT}-GFP had the highest activity, while $CBP_{\Delta IDR6}$-GFP and $CBP_{\Delta IDR7}$-GFP showed reduced acetylation (Figures 4O and S4R). This disparity suggests that the high H3K27ac levels seen in $CBP_{\Delta IDR6}$-GFP cells are not due to intrinsic catalytic gains. Instead, the formation of larger condensates could increase CBP-chromatin contacts or provide a cellular stimulus for activity that is lost during *in vitro* purification.

CBP IDRs shape how CBP binds to chromatin

Our results suggest that CBP-IDRs outside the HAT domain influence catalytic activity, revealing a discrepancy between *in vitro* behavior and cellular histone acetylation levels. We hypothesized that CBP-IDRs regulate total acetylation by modulating both HAT activity and chromatin association via condensate formation. To test this, we performed chromatin immunoprecipitation sequencing (ChIP-seq) and CUT&RUN on our inducible CBP-GFP lines.

To confirm that the GFP tag does not disrupt chromatin recruitment, we compared the ChIP-seq profiles of endogenous CBP in maternal HEK293T cells (α-CBP; $CBP_{WT\text{-}Tet3G}$) and inducible CBP-GFP (α-GFP; Figure 4L). Genome-wide read densities correlated strongly (Figures S5A and S5B); 7,661 identified CBP-GFP binding sites significantly overlapped with endogenous CBP sites (Figures 5A and S5F). While we detected fewer peaks for CBP-GFP than for endogenous CBP (14,913), we attribute this to lower ChIP efficiency, likely due to antibody differences and the presence of competing endogenous CBP. Accordingly, while endogenous $CBP_{WT\text{-}Tet3G}$ binding sites were still enriched for CBP_{WT}-GFP read densities in GFP ChIP-seq data, the enrichment was lower than that observed with endogenous $CBP_{WT\text{-}Tet3G}$ read densities from CBP ChIP-seq data (Figures S5C and S5D); endogenous $CBP_{WT\text{-}Tet3G}$ sites (median width = 416 bp) were therefore broader than those of CBP_{WT}-GFP (median width = 340 bp; Figure 5B), again indicative of differences in ChIP efficiency. CBP-GFP exhibited near-identical genomic distribution to $CBP_{WT\text{-}Tet3G}$, primarily targeting promoters (~52%), introns, and intergenic regions (Figure 5C). CBP-GFP binding sites were closer than expected by chance[44] (Figures S5E and S5F). Together, these results confirm that CBP-GFP accurately recapitulates the binding patterns of endogenous CBP.

Given the differences in ChIP efficiency, we focused on CBP-GFP ChIP-seq data to uncover how CBP-IDRs affected chromatin localization. Surprisingly, both $CBP_{\Delta IDR6}$-GFP (18,357 sites) and $CBP_{\Delta IDR7}$-GFP (17,237 sites) exhibited more than double the binding sites of CBP_{WT}-GFP (7,661 sites; Figure 5A). This increase was accompanied by a shift toward introns and intergenic regions (Figure 5C). While CBP_{WT}-GFP sites largely overlapped with both mutants (69%–77%), only 43% of $CBP_{\Delta IDR7}$-GFP sites overlapped with $CBP_{\Delta IDR6}$-GFP (Figures 5A and S5F).

We next examined how CBP-IDRs influenced chromatin binding profiles. At endogenous sites, $CBP_{\Delta IDR6}$-GFP showed enriched read densities and wider median peaks (394 bp vs. 340 bp for CBP_{WT}-GFP), while $CBP_{\Delta IDR7}$-GFP was depleted with narrower peaks (283 bp; Figures 5B, S5C, and S5D). These genomic profiles mirror our imaging data: the larger condensates formed by $CBP_{\Delta IDR6}$-GFP enhance chromatin enrichment and peak size, whereas more dispersed $CBP_{\Delta IDR7}$-GFP results in reduced binding levels across a higher number of locations.

CBP IDRs shape histone acetylation

To determine how chromatin localization influences acetylation, we performed spike-in normalized CUT&RUN for H3K27ac. Representative loci, such as *TSC22D3*, confirmed that CBP-GFP occupies endogenous sites and promotes corresponding H3K27ac enrichment (Figure 5D). Deleting CBP-IDRs significantly altered the H3K27ac landscape. $CBP_{\Delta IDR6}$-GFP increased both the number (46,576 vs. 37,117) and median width (421 bp vs. 381 bp) of H3K27ac domains compared to CBP_{WT}-GFP (Figure 5E). Conversely, $CBP_{\Delta IDR7}$-GFP caused a drastic reduction in the number of H3K27ac loci (9,213), though peak width remained stable (Figure 5E). These changes in H3K27ac levels (Figure 5F) directly correlated with CBP-GFP enrichment at these sites (Figures 5G, S5G, and S5H), indicating that IDR-driven localization is a primary determinant of genomic acetylation patterns.

To compare how CBP-IDRs affect acetylation without complexities from mixtures of CBP-bound and CBP-unbound sites, we analyzed 4,765 common loci shared by all datasets (Figure 5A, magenta). At these sites, $CBP_{\Delta IDR6}$-GFP showed enrichment for both CBP-GFP and H3K27ac compared to CBP_{WT}-GFP (Figures 5H, 5I, and S5I). Notably, while $CBP_{\Delta IDR7}$-GFP read densities were also slightly higher than CBP_{WT}-GFP (mean 0.18 vs. 0.17), they were depleted for H3K27ac. Although CBP-GFP data were not normalized to

(B) Peak widths of CBP binding sites. *p* values from Mann-Whitney U test.
(C) Distribution of CBP binding sites by genome region.
(D) Genome browser views of CBP and GFP ChIP-seq (top) and H3K27ac CUT&RUN (bottom) at the *TSC22D3* gene. Solid bars show binding sites identified using MACS2.
(E) Peak widths of enriched H3K27ac domains. *p* values from Mann-Whitney U test.
(F and G) Read density enrichment at H3K27ac domains. (F) H3K27ac and (G) CBP-GFP. H3K27ac peaks were randomly downsampled to match the smallest dataset (CBP_{WT}-GFP, 9,213). *p* values from Mann-Whitney U test.
(H and I) Read density enrichment at 4,657 CBP peaks common in all datasets. (H) H3K27ac and (I) CBP-GFP. *p* values from Mann-Whitney U test.
(J) Distribution of common and unique CBP binding sites.
(K and L) CBP-GFP enrichment at unique sites. (K) CBP-GFP and (L) H3K27ac. Heatmaps show ±2.5 kb from center of peaks for CBP_{WT}-GFP (3,049 sites), $CBP_{\Delta IDR6}$-GFP (13,776 sites), and CBP_{IDR7}-GFP (12,605 sites).
(M and N) Enrichment of (M) CBP-GFP and (N) H3K27ac read densities at 2,348,854 GRCh38 cCREs.[45] *p* values from Mann-Whitney U test. *p* values reported as absolute values or $^*p < 0.05$, $^{**}p < 0.01$, and $^{***}p < 0.001$. Boxplots show median (center line) and first and third quartiles (box). Whiskers extend to 1.5× the interquartile range; individual data points represent outliers.
See also Figure S5.

spike-in controls, this suggests that while H3K27ac levels broadly reflect CBP recruitment for the CBP_{WT}-GFP and $CBP_{\Delta IDR6}$-GFP constructs, a discrepancy exists between $CBP_{\Delta IDR7}$-GFP recruitment and H3K27ac.

We mapped the genomic distribution of unique binding sites for each construct. While shared sites predominantly occupied promoters (58%) and exons (22%), unique sites for CBP_{WT}-GFP, $CBP_{\Delta IDR6}$-GFP, and $CBP_{\Delta IDR7}$-GFP shifted toward introns and intergenic regions (Figure 5J). This suggests that both enhanced condensation ($CBP_{\Delta IDR6}$-GFP) and condensate dispersal ($CBP_{\Delta IDR7}$-GFP) drive CBP relocation to non-promoter regions. At these unique sites, both mutants showed higher CBP-GFP occupancy than CBP_{WT}-GFP (Figures 5K and S5J). However, H3K27ac levels remained high only at unique $CBP_{\Delta IDR6}$-GFP sites and were depleted at $CBP_{\Delta IDR7}$-GFP sites (Figures 5L and S5K). This reinforces that while both CBP-IDR deletions expand CBP's genomic footprint, only CBP_{IDR6}-mediated condensation supports effective acetylation at these new locations.

Finally, we assessed recruitment and H3K27ac levels at ENCODE-defined candidate *cis*-regulatory elements (cCREs).[45] Compared to CBP_{WT}-GFP, $CBP_{\Delta IDR6}$-GFP was enriched for both binding and H3K27ac, while $CBP_{\Delta IDR6}$-GFP was depleted (Figures 5M and 5N).

These data demonstrate that CBP-IDRs dictate genomic histone acetylation patterns by modulating the interplay between HAT activity and chromatin localization, a regulatory mechanism consistently observed at cCREs genome-wide.

CBP-IDRs affect gene expression

Our results show that CBP-IDRs regulate condensate properties, thereby shaping CBP chromatin localization and histone acetylation. To determine if these changes affect transcription, we performed RNA-seq on our inducible CBP_{WT}-GFP, $CBP_{\Delta IDR6}$-GFP, and $CBP_{\Delta IDR7}$-GFP lines. Replicates clustered distinctly by genotype in principal-component analysis (PCA; Figures S6A and S6B). Compared to CBP_{WT}-GFP, $CBP_{\Delta IDR6}$-GFP significantly deregulated 539 genes (190 up, 349 down), while $CBP_{\Delta IDR7}$-GFP lines deregulated 460 genes (182 up, 278 down; Figures 6A, 6B, S6C, and S6D). These expression changes correlated with altered CBP binding and H3K27ac levels. For example, *HAND1* was upregulated in both mutants, coinciding with additional CBP-GFP recruitment and shifting H3K27ac patterns at its regulatory elements (Figure 6C). Collectively, these data show that disrupting CBP-IDRs triggers off-target CBP accumulation and H3K27ac alterations, leading to widespread transcriptional deregulation.

DISCUSSION

To regulate transcription, molecular condensates must maintain optimal biophysical properties.[11,46–48] We demonstrate that CBP maintains this balance via the opposing contributions of CBP_{IDR6} and CBP_{IDR7}, which function through sequence patterning and amino acid composition, respectively (Figures 7A and S7). This internal regulation mirrors balancing activities observed in other proteins like Ataxin-2.[49] While CBP is recruited to chromatin via C-terminal TF interactions,[50] disrupting CBP_{IDR6} and CBP_{IDR7} alters CBP's post-recruitment behavior, likely by modifying its interactions within TF condensates. These disruptions increase CBP binding site frequency and alter recruitment profiles in a manner that mirrors the changes observed in isolated CBP condensates. Ultimately, this changes histone acetylation at CREs and alters gene expression. Given CBP's role as a scaffold, such biophysical modifications likely further disrupt the recruitment and retention of additional regulatory factors.[51]

Beyond biophysical stability, CBP-IDRs determine the sensitivity of these condensates to lysine acetylation. While p300 condensates are regulated by global acetylation through bromodomain recruitment[11,40] and inhibited by direct auto-acetylation,[20] CBP remains relatively buffered against global acetylation changes (Figure 7B). This buffering capacity appears mediated by CBP_{IDR6}, the deletion of which hypersensitizes CBP to global acetyl-lysine changes. Furthermore, while acetylation of CBP_{AL} negatively regulates condensate size and frequency, this inhibitory effect is dependent upon the integrity of C-terminal IDRs (Figure 7B). Taken together, the results highlight the fundamental importance of CBP-IDRs to condensate behavior but also underline the complex nature of CBP condensates, which integrate diverse environmental factors including global and direct lysine acetylation on CBP.

Unexpectedly, disrupting CBP-IDRs also alters CBP's catalytic activity. Given that the $p300_{TAZ2}$ domain negatively regulates HAT activity[52] and that CBP_{TAZ2} remains intact in our $CBP_{\Delta IDR6}$ and $CBP_{\Delta IDR7}$ mutants, we speculate that CBP_{IDR6} and CBP_{IDR7} normally relieve CBP_{TAZ2}-mediated inhibition; their removal may consequently allow CBP_{TAZ2} to suppress HAT activity. This suggests that factors binding to C-terminal CBP-IDRs can modulate CBP activity by influencing CBP-IDR behavior. For instance, the adenovirus protein *early region 1A* (*E1A*) inhibits HAT activity only when interacting with a region overlapping CBP_{IDR6}; similarly, *activator of thyroid and retinoic acid receptor* (ACTR) mutants associating with C-terminal domain CBP_{NCBD} stimulate HAT activity, whereas CREB binding at the N-terminal CBP_{KIX} domain does not.[21]

These findings have significant implications for the deregulation of CBP in disease. Many variants associated with developmental disorders like Rubinstein-Taybi (RTS) and Menke-Hennekam (MHS) syndromes, as well as B cell lymphoma, map directly to the CBP-IDRs characterized here.[53–55] Given that mutations in IDRs can drive disease by altering condensate formation,[56] the roles we define for CBP-IDRs suggest potential mechanisms for disease etiology. Indeed, because many of these conditions are heterozygous, the ability of mutant CBP-IDRs to exert dominant effects on endogenous condensates via disrupted homotypic interactions may be particularly relevant. Furthermore, we observe significant sequence divergence between the functional IDRs of CBP and p300, which likely explains their contrasting responses to A-485.[11] Although not tested here, it is possible that these less well conserved but functionally important domains could form the basis for functional specialization of CBP and p300.

Limitations of the study

While our study provides key insights into CBP-IDR function, several limitations remain. First, because endogenous CBP

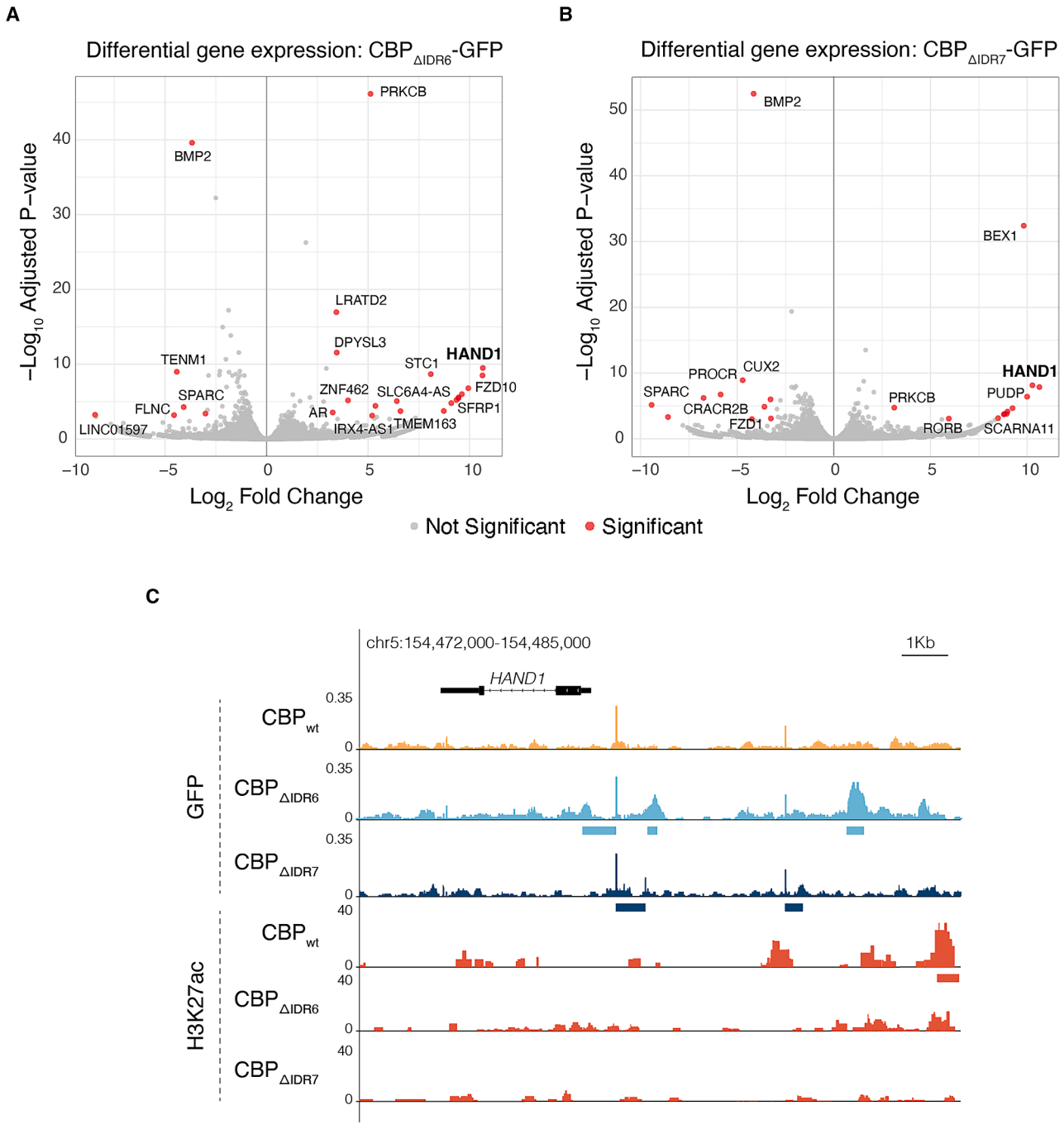

Figure 6. CBP-IDRs regulate gene expression profiles

(A and B) Differentially expressed genes between (A) CBP_{WT}-GFP and $CBP_{\Delta IDR6}$-GFP and (B) CBP_{WT}-GFP and $CBP_{\Delta IDR7}$-GFP. Genes showing significant changes in expression ($p < 0.001$ and $\log_2FC > 3$) are highlighted (red points, gene names, and Table S4). HAND1 (bold) is upregulated in both datasets.
(C) Genome browser views of GFP ChIP-seq (top) and H3K27ac CUT&RUN (bottom) at the *HAND1* gene. Solid bars show identified binding sites.
See also Figure S6.

was not depleted, we cannot exclude complexities arising from mixed populations of mutant and WT proteins. Although CBP-IDR mutations clearly alter endogenous CBP condensate behavior (Figures 2L–2O), our study did not investigate their impact on heterotypic interaction networks. Given the multi-component nature of condensates, it is likely that broader networks are similarly disrupted, and changes in H3K27ac may be complicated by recruitment of endogenous CBP and p300 to the same genomic loci. Second, transient co-expression can lead to varying protein levels due to differences in

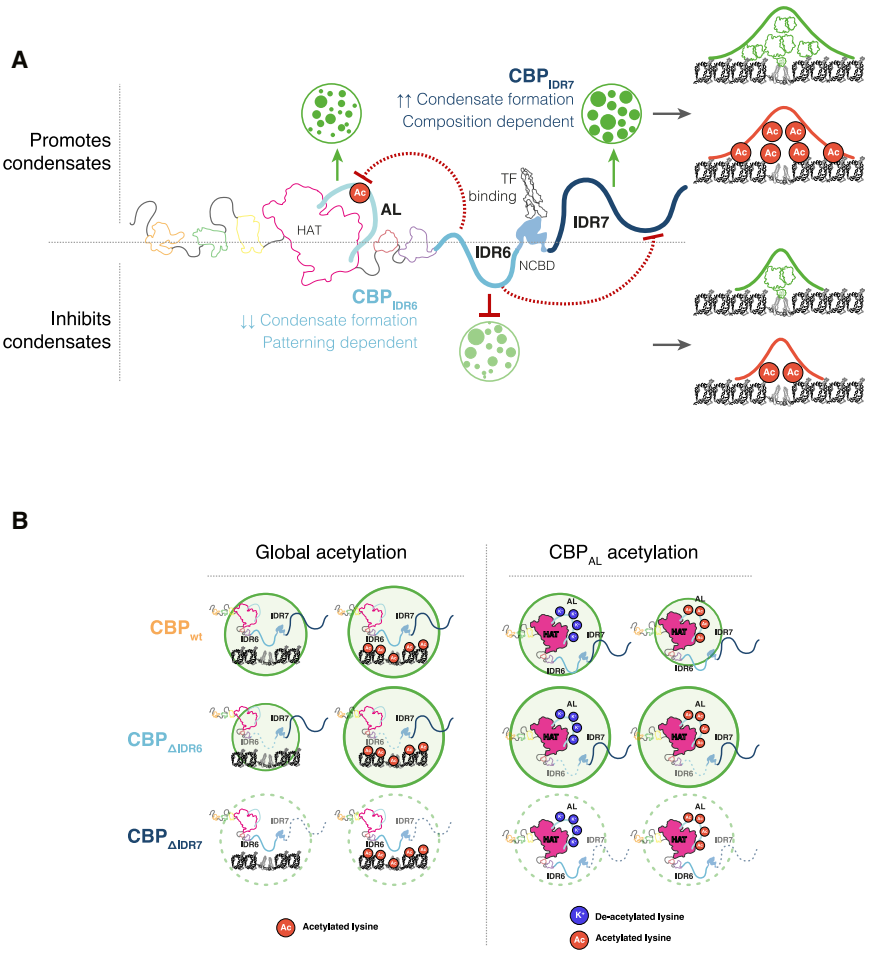

Figure 7. Summary of CBP-IDR functions

(A) Summary of how CBP-IDRs regulate condensates, chromatin localization, and histone acetylation.

(B) Summary of how CBP-IDRs work with lysine acetylation to control condensate behavior.

See also Figure S7.

transfection efficiency, which could cause differences in condensates, although we note that inducible near-endogenous expression displayed consistent behavior (Figure 4M). Thirdly, we cannot exclude that observed phenotypes result from altered TF binding or changes to specific PTMs on CBP-IDRs. Nevertheless, while disrupted folding of CBP_{NCBD} might influence condensate behavior, similar deletions in p300 show only minimal effects on chromatin association.[50]

Finally, interpreting experiments involving CBP_{AL} is challenging due to its diverse roles. CBP_{AL} is a critical RNA-binding site[15]; given the importance of RNA in condensate formation[43] and our data confirming that RNA helps maintain CBP condensates, disrupted RNA binding could also alter condensate properties. Additionally, CBP_{AL} acetylation directly regulates CBP's catalytic activity,[17] which may indirectly influence condensates by altering global acetylation levels.[6,40]

CBP is essential for integrating environmental signals to generate precise histone acetylation profiles and scaffold transcriptional complexes to regulate gene expression. Our work highlights how CBP-IDRs facilitate this process by tuning condensate properties and modulating responses to lysine acetylation. Together, these findings underscore the necessity of characterizing the unique behaviors of IDRs within multivalent co-activators to fully understand their roles in gene regulation and disease.

RESOURCE AVAILABILITY

Lead contact

Requests for further information and resources should be directed to and will be fulfilled by the lead contact, Daniel A. Bose (d.bose@sheffield.ac.uk).

Materials availability

Plasmids generated in this study have been deposited with Addgene under the Daniel A. Bose laboratory collection (Addgene deposit #84398). All unique/stable reagents generated in this study are available from the lead contact without restriction.

Data and code availability

- Sequencing data have been deposited to the Gene Expression Omnibus (GEO) database (https://www.ncbi.nlm.nih.gov/geo/) grouped under SuperSeries GEO: GSE299618 and are available immediately. Accession numbers are listed in the key resources table. All other data reported in this paper will be shared by the lead contact upon request.
- This paper does not report original code.
- Any additional information required to reanalyze the data reported in this paper is available from the lead contact upon request.

ACKNOWLEDGMENTS

D.A.B. and A.E.T. are funded by the Wellcome Trust and Royal Society (213501/Z/18/Z and 220192/Z/20/Z); K.L.G., D.A.B., A.E.T., and T.D.C. received a BBSRC Pioneer Award (BB/Y513453/1); K.L.G. was supported by BB/M011151/1; L.J.H. was supported by MR/N013840; N.A.C. and G.G. were funded by UoS,;and T.D.C. was supported by BB/T008032/1. We thank Susan Clark (flow cytometry), UoS High Performance Computing, and Wolfson Light Microscopy Facility. Nikon W1 was funded by BB/V019368/1. This research was funded in whole, or in part, by the Wellcome Trust (213501/Z/18/Z and 220192/Z/20/Z). For the purpose of open access, the author has applied a CC-BY public copyright license to any author-accepted manuscript version arising from this submission.

AUTHOR CONTRIBUTIONS

The study was conceived and led by D.A.B., A.E.T., T.D.C., and K.L.G. D.A.B., A.E.T., and K.L.G. designed and led experiments with further input from N.A.C., G.G., L.J.H., B.V.E., T.I.E., and S.S.B. L.J.H., M.D., and D.A.B. analyzed next-generation sequencing data. D.A.B., K.L.G., and A.E.T. wrote the manuscript. All authors reviewed and commented on the manuscript.

DECLARATION OF INTERESTS

T.D.C. is the founder and CEO of Exciting Instruments, a company that develops and sells instrumentation for single-molecule fluorescence experiments, including smFRET.

DECLARATION OF GENERATIVE AI AND AI-ASSISTED TECHNOLOGIES IN THE WRITING PROCESS

During the preparation of this work, the authors used Google Gemini for minor text edits. After using this tool or service, the authors reviewed and edited the content as needed and take full responsibility for the content of the publication.

STAR★METHODS

Detailed methods are provided in the online version of this paper and include the following:

- KEY RESOURCES TABLE
- EXPERIMENTAL MODEL AND STUDY PARTICIPANT DETAILS
  - Cell culture
- METHOD DETAILS
  - Cell culture and maintenance
  - Molecular biology and cloning
  - Construction of stably integrated CBP-Halotag cell lines
  - Imaging
  - Immunofluorescence and fixed cell imaging
  - Western blotting
  - Histone acetyltransferase assay
  - Chromatin immunoprecipitation (CHIP)
  - Cleavage under targets and release using nuclease (CUT&RUN)
  - RNA-seq
  - Computational analysis
- QUANTIFICATION AND STATISTICAL ANALYSIS
  - Image analysis
  - ChIP-seq data analysis
  - CUT&RUN data analysis
  - RNA-seq data analysis
  - Statistical analysis

SUPPLEMENTAL INFORMATION

Supplemental information can be found online at https://doi.org/10.1016/j.celrep.2026.117109.

Received: July 9, 2025
Revised: December 15, 2025
Accepted: February 18, 2026

REFERENCES

1. Holehouse, A.S., and Kragelund, B.B. (2023). The molecular basis for cellular function of intrinsically disordered protein regions. Nat. Rev. Mol. Cell Biol. *25*, 187–211.
2. van der Lee, R., Buljan, M., Lang, B., Weatheritt, R.J., Daughdrill, G.W., Dunker, A.K., Fuxreiter, M., Gough, J., Gsponer, J., Jones, D.T., et al. (2014). Classification of intrinsically disordered regions and proteins. Chem. Rev. *114*, 6589–6631.
3. Lobel, J.H., and Ingolia, N.T. (2025). Deciphering disordered regions controlling mRNA decay in high-throughput. Nature *642*, 805–813.
4. Moses, D., Guadalupe, K., Yu, F., Flores, E., Perez, A.R., McAnelly, R., Shamoon, N.M., Kaur, G., Cuevas-Zepeda, E., Merg, A.D., et al. (2024). Structural biases in disordered proteins are prevalent in the cell. Nat. Struct. Mol. Biol. *31*, 283–292. https://doi.org/10.1038/s41594-023-01148-8.
5. Cuevas-Velazquez, C.L., Vellosillo, T., Guadalupe, K., Schmidt, H.B., Yu, F., Moses, D., Brophy, J.A.N., Cosio-Acosta, D., Das, A., Wang, L., et al. (2021). Intrinsically disordered protein biosensor tracks the physical-chemical effects of osmotic stress on cells. Nat. Commun. *12*, 5438.
6. Narita, T., Ito, S., Higashijima, Y., Chu, W.K., Neumann, K., Walter, J., Satpathy, S., Liebner, T., Hamilton, W.B., Maskey, E., et al. (2021). Enhancers are activated by p300/CBP activity-dependent PIC assembly, RNAPII recruitment, and pause release. Mol. Cell *81*, 2166–2182.e6. https://doi.org/10.1016/j.molcel.2021.03.008.
7. Hunt, G., Boija, A., and Mannervik, M. (2022). p300/CBP sustains Polycomb silencing by non-enzymatic functions. Mol. Cell *82*, 3580–3597.e9.
8. Weinert, B.T., Narita, T., Satpathy, S., Srinivasan, B., Hansen, B.K., Schölz, C., Hamilton, W.B., Zucconi, B.E., Wang, W.W., Liu, W.R., et al. (2018). Time-resolved analysis reveals rapid dynamics and broad scope of the CBP/p300 acetylome. Cell *174*, 231–244.e12.
9. Tropberger, P., Pott, S., Keller, C., Kamieniarz-Gdula, K., Caron, M., Richter, F., Li, G., Mittler, G., Liu, E.T., Bühler, M., et al. (2013). Regulation of transcription through acetylation of H3K122 on the lateral surface of the histone octamer. Cell *152*, 859–872.
10. Tie, F., Banerjee, R., Stratton, C.A., Prasad-Sinha, J., Stepanik, V., Zlobin, A., Diaz, M.O., Scacheri, P.C., and Harte, P.J. (2009). CBP-mediated acetylation of histone H3 lysine 27 antagonizes Drosophila Polycomb silencing. Development *136*, 3131–3141.
11. Ma, L., Gao, Z., Wu, J., Zhong, B., Xie, Y., Huang, W., and Lin, Y. (2021). Co-condensation between transcription factor and coactivator p300 modulates transcriptional bursting kinetics. Mol. Cell *81*, 1682–1697.e7. https://doi.org/10.1016/j.molcel.2021.01.031.
12. Dyson, H.J., and Wright, P.E. (2016). Role of Intrinsic Protein Disorder in the Function and Interactions of the Transcriptional Coactivators CREB-binding Protein (CBP) and p300. J. Biol. Chem. *291*, 6714–6722.
13. Sturzenegger, F., Zosel, F., Holmstrom, E.D., Buholzer, K.J., Makarov, D.E., Nettels, D., and Schuler, B. (2018). Transition path times of coupled folding and binding reveal the formation of an encounter complex. Nat. Commun. *9*, 4708.
14. Demarest, S.J., Martinez-Yamout, M., Chung, J., Chen, H., Xu, W., Dyson, H.J., Evans, R.M., and Wright, P.E. (2002). Mutual synergistic folding in recruitment of CBP/p300 by p160 nuclear receptor coactivators. Nature *415*, 549–553.
15. Bose, D.A., Donahue, G., Reinberg, D., Shiekhattar, R., Bonasio, R., and Berger, S.L. (2017). RNA binding to CBP stimulates histone acetylation and transcription. Cell *168*, 135–149.e22.

16. Hou, T.Y., and Kraus, W.L. (2022). Analysis of estrogen-regulated enhancer RNAs identifies a functional motif required for enhancer assembly and gene expression. Cell Rep. *39*, 110944.

17. Thompson, P.R., Wang, D., Wang, L., Fulco, M., Pediconi, N., Zhang, D., An, W., Ge, Q., Roeder, R.G., Wong, J., et al. (2004). Regulation of the p300 HAT domain via a novel activation loop. Nat. Struct. Mol. Biol. *11*, 308–315.

18. Ortega, E., Rengachari, S., Ibrahim, Z., Hoghoughi, N., Gaucher, J., Holehouse, A.S., Khochbin, S., and Panne, D. (2018). Transcription factor dimerization activates the p300 acetyltransferase. Nature *562*, 538–544.

19. Thompson, P.R., Kurooka, H., Nakatani, Y., and Cole, P.A. (2001). Transcriptional coactivator protein p300. Kinetic characterization of its histone acetyltransferase activity. J. Biol. Chem. *276*, 33721–33729.

20. Zhang, Y., Brown, K., Yu, Y., Ibrahim, Z., Zandian, M., Xuan, H., Ingersoll, S., Lee, T., Ebmeier, C.C., Liu, J., et al. (2021). Nuclear condensates of p300 formed though the structured catalytic core can act as a storage pool of p300 with reduced HAT activity. Nat. Commun. *12*, 4618.

21. Perissi, V., Dasen, J.S., Kurokawa, R., Wang, Z., Korzus, E., Rose, D.W., Glass, C.K., and Rosenfeld, M.G. (1999). Factor-specific modulation of CREB-binding protein acetyltransferase activity. Proc. Natl. Acad. Sci. USA *96*, 3652–3657.

22. Boisvert, F.M., Kruhlak, M.J., Box, A.K., Hendzel, M.J., and Bazett-Jones, D.P. (2001). The transcription coactivator CBP is a dynamic component of the promyelocytic leukemia nuclear body. J. Cell Biol. *152*, 1099–1106.

23. LaMorte, V.J., Dyck, J.A., Ochs, R.L., and Evans, R.M. (1998). Localization of nascent RNA and CREB binding protein with the PML-containing nuclear body. Proc. Natl. Acad. Sci. USA *95*, 4991–4996.

24. Jones, D.T., and Cozzetto, D. (2015). DISOPRED3: precise disordered region predictions with annotated protein-binding activity. Bioinformatics *31*, 857–863.

25. Xue, B., Dunbrack, R.L., Williams, R.W., Dunker, A.K., and Uversky, V.N. (2010). PONDR-FIT: a meta-predictor of intrinsically disordered amino acids. Biochim. Biophys. Acta *1804*, 996–1010.

26. Jumper, J., Evans, R., Pritzel, A., Green, T., Figurnov, M., Ronneberger, O., Tunyasuvunakool, K., Bates, R., Žídek, A., Potapenko, A., et al. (2021). Highly accurate protein structure prediction with AlphaFold. Nature *596*, 583–589.

27. Wang, X., Arai, S., Song, X., Reichart, D., Du, K., Pascual, G., Tempst, P., Rosenfeld, M.G., Glass, C.K., and Kurokawa, R. (2008). Induced ncRNAs allosterically modify RNA-binding proteins in cis to inhibit transcription. Nature *454*, 126–130.

28. Ruff, K.M., King, M.R., Ying, A.W., Liu, V., Pant, A., Lieberman, W.E., Shinn, M.K., Su, X., Kadoch, C., and Pappu, R.V. (2026). Molecular grammars of predicted intrinsically disordered regions that span the human proteome. Cell *189*, 323–342.e17. https://doi.org/10.1016/j.cell.2025.10.019.

29. King, M.R., Ruff, K.M., Lin, A.Z., Pant, A., Farag, M., Lalmansingh, J.M., Wu, T., Fossat, M.J., Ouyang, W., Lew, M.D., et al. (2024). Macromolecular condensation organizes nucleolar sub-phases to set up a pH gradient. Cell *187*, 1889–1906.e24.

30. Rodríguez, C.S., and Laurents, D.V. (2024). Architectonic principles of polyproline II helix bundle protein domains. Arch. Biochem. Biophys. *756*, 109981.

31. Piai, A., Calçada, E.O., Tarenzi, T., Grande, A.D., Varadi, M., Tompa, P., Felli, I.C., and Pierattelli, R. (2016). Just a Flexible Linker? The Structural and Dynamic Properties of CBP-ID4 Revealed by NMR Spectroscopy. Biophys. J. *110*, 372–381.

32. Shin, Y., Berry, J., Pannucci, N., Haataja, M.P., Toettcher, J.E., and Brangwynne, C.P. (2017). Spatiotemporal Control of Intracellular Phase Transitions Using Light-Activated optoDroplets. Cell *168*, 159–171.e14.

33. Delvecchio, M., Gaucher, J., Aguilar-Gurrieri, C., Ortega, E., and Panne, D. (2013). Structure of the p300 catalytic core and implications for chromatin targeting and HAT regulation. Nat. Struct. Mol. Biol. *20*, 1040–1046. https://doi.org/10.1038/nsmb.2642.

34. Riback, J.A., Zhu, L., Ferrolino, M.C., Tolbert, M., Mitrea, D.M., Sanders, D.W., Wei, M.-T., Kriwacki, R.W., and Brangwynne, C.P. (2020). Composition-dependent thermodynamics of intracellular phase separation. Nature *581*, 209–214. https://doi.org/10.1038/s41586-020-2256-2.

35. Holehouse, A.S., Das, R.K., Ahad, J.N., Richardson, M.O.G., and Pappu, R.V. (2017). CIDER: Resources to analyze sequence-ensemble relationships of intrinsically disordered proteins. Biophys. J. *112*, 16–21.

36. Martin, E.W., Holehouse, A.S., Grace, C.R., Hughes, A., Pappu, R.V., and Mittag, T. (2016). Sequence Determinants of the Conformational Properties of an Intrinsically Disordered Protein Prior to and upon Multisite Phosphorylation. J. Am. Chem. Soc. *138*, 15323–15335.

37. Lancaster, A.K., Nutter-Upham, A., Lindquist, S., and King, O.D. (2014). PLAAC: a web and command-line application to identify proteins with prion-like amino acid composition. Bioinformatics *30*, 2501–2502.

38. Hunter, K., Brandt, T., Guadalupe, K., Kolamunna, K., Lotthammer, J.M., Shamoon, N.M., Nicholson, B., Day, L., Martinez, A., Holehouse, A.S., et al. (2026). Rational design of disordered proteins for systematic sequence-to-function investigation. Preprint at bioRxiv. https://doi.org/10.1101/2023.10.29.564547.

39. Wang, J., Choi, J.-M., Holehouse, A.S., Lee, H.O., Zhang, X., Jahnel, M., Maharana, S., Lemaitre, R., Pozniakovsky, A., Drechsel, D., et al. (2018). A molecular grammar governing the driving forces for phase separation of prion-like RNA binding proteins. Cell *174*, 688–699.e16.

40. Ibrahim, Z., Wang, T., Destaing, O., Salvi, N., Hoghoughi, N., Chabert, C., Rusu, A., Gao, J., Feletto, L., Reynoird, N., et al. (2022). Structural insights into p300 regulation and acetylation-dependent genome organisation. Nat. Commun. *13*, 7759.

41. Lasko, L.M., Jakob, C.G., Edalji, R.P., Qiu, W., Montgomery, D., Digiammarino, E.L., Hansen, T.M., Risi, R.M., Frey, R., Manaves, V., et al. (2017). Discovery of a selective catalytic p300/CBP inhibitor that targets lineage-specific tumours. Nature *550*, 128–132.

42. Yi, F., Cai, C., Ruan, B., Hao, M., Yeo, S.K., Haas, M., Yang, F., Zhang, X., and Guan, J.-L. (2023). Regulation of RB1CC1/FIP200 stability and autophagy function by CREBBP-mediated acetylation in an intrinsically disordered region. Autophagy *19*, 1662–1677.

43. Henninger, J.E., Oksuz, O., Shrinivas, K., Sagi, I., LeRoy, G., Zheng, M.M., Andrews, J.O., Zamudio, A.V., Lazaris, C., Hannett, N.M., et al. (2021). RNA-mediated feedback control of transcriptional condensates. Cell *184*, 207–225.e24. https://doi.org/10.1016/j.cell.2020.11.030.

44. Favorov, A., Mularoni, L., Cope, L.M., Medvedeva, Y., Mironov, A.A., Makeev, V.J., and Wheelan, S.J. (2012). Exploring massive, genome scale datasets with the GenometriCorr package. PLoS Comput. Biol. *8*, e1002529.

45. The ENCODE Project Consortium; Moore, J.E., Purcaro, M.J., Pratt, H.E., Epstein, C.B., Shoresh, N., Adrian, J., Kawli, T., Davis, C.A., Dobin, A., et al. (2020). Expanded encyclopaedias of DNA elements in the human and mouse genomes. Nature *583*, 699–710.

46. Chong, S., Graham, T.G.W., Dugast-Darzacq, C., Dailey, G.M., Darzacq, X., and Tjian, R. (2022). Tuning levels of low-complexity domain interactions to modulate endogenous oncogenic transcription. Mol. Cell *82*, 2084–2097.e5.

47. He, J., Huo, X., Pei, G., Jia, Z., Yan, Y., Yu, J., Qu, H., Xie, Y., Yuan, J., Zheng, Y., et al. (2024). Dual-role transcription factors stabilize intermediate expression levels. Cell *187*, 2746–2766.e25. https://doi.org/10.1016/j.cell.2024.03.023.

48. Trojanowski, J., Frank, L., Rademacher, A., Mücke, N., Grigaitis, P., and Rippe, K. (2022). Transcription activation is enhanced by multivalent interactions independent of phase separation. Mol. Cell *82*, 1878–1893.e10.

49. Boeynaems, S., Dorone, Y., Zhuang, Y., Shabardina, V., Huang, G., Marian, A., Kim, G., Sanyal, A., Şen, N.-E., Griffith, D., et al. (2023).

Poly(A)-binding protein is an ataxin-2 chaperone that regulates biomolecular condensates. Mol. Cell *83*, 2020–2034.e6. https://doi.org/10.1016/j.molcel.2023.05.025.

50. Ferrie, J.J., Karr, J.P., Graham, T.G.W., Dailey, G.M., Zhang, G., Tjian, R., and Darzacq, X. (2024). p300 is an obligate integrator of combinatorial transcription factor inputs. Mol. Cell *84*, 234–243.e4.
51. Boija, A., Klein, I.A., Sabari, B.R., Dall'Agnese, A., Coffey, E.L., Zamudio, A.V., Li, C.H., Shrinivas, K., Manteiga, J.C., Hannett, N.M., et al. (2018). Transcription Factors Activate Genes through the Phase-Separation Capacity of Their Activation Domains. Cell *175*, 1842–1855.e16.
52. Xu, L., Xuan, H., He, W., Zhang, L., Huang, M., Li, K., Wen, H., Xu, H., and Shi, X. (2023). TAZ2 truncation confers overactivation of p300 and cellular vulnerability to HDAC inhibition. Nat. Commun. *14*, 5362. https://doi.org/10.1038/s41467-023-41245-2.
53. Petrij, F., Giles, R.H., Dauwerse, H.G., Saris, J.J., Hennekam, R.C., Masuno, M., Tommerup, N., van Ommen, G.J., Goodman, R.H., and Peters, D.J. (1995). Rubinstein-Taybi syndrome caused by mutations in the transcriptional co-activator CBP. Nature *376*, 348–351.
54. Haghshenas, S., Bout, H.J., Schijns, J.M., Levy, M.A., Kerkhof, J., Bhai, P., McConkey, H., Jenkins, Z.A., Williams, E.M., Halliday, B.J., et al. (2024). Menke-Hennekam syndrome; delineation of domain-specific subtypes with distinct clinical and DNA methylation profiles. HGG Adv. *5*, 100337.
55. Pasqualucci, L., Dominguez-Sola, D., Chiarenza, A., Fabbri, G., Grunn, A., Trifonov, V., Kasper, L.H., Lerach, S., Tang, H., Ma, J., et al. (2011). Inactivating mutations of acetyltransferase genes in B-cell lymphoma. Nature *471*, 189–195.
56. Mensah, M.A., Niskanen, H., Magalhaes, A.P., Basu, S., Kircher, M., Sczakiel, H.L., Reiter, A.M.V., Elsner, J., Meinecke, P., Biskup, S., et al. (2023). Aberrant phase separation and nucleolar dysfunction in rare genetic diseases. Nature *614*, 564–571.
57. Conant, D., Hsiau, T., Rossi, N., Oki, J., Maures, T., Waite, K., Yang, J., Joshi, S., Kelso, R., Holden, K., et al. (2022). Inference of CRISPR edits from Sanger trace data. CRISPR J *5*, 123–130.
58. Schindelin, J., Arganda-Carreras, I., Frise, E., Kaynig, V., Longair, M., Pietzsch, T., Preibisch, S., Rueden, C., Saalfeld, S., Schmid, B., et al. (2012). Fiji: an open-source platform for biological-image analysis. Nat. Methods *9*, 676–682.
59. Thévenaz, P., Ruttimann, U.E., and Unser, M. (1998). A pyramid approach to subpixel registration based on intensity. IEEE Trans. Image Process. *7*, 27–41.
60. R Core Team (2021). R: A Language and Environment for Statistical Computing (R Foundation for Statistical Computing).
61. R Studio Team (2015). RStudio: Integrated Development for R (R Foundation for Statistical Computing).
62. Martin, M. (2011). Cutadapt removes adapter sequences from high-throughput sequencing reads. EMBnet J. *17*, 10.
63. Li, H., and Durbin, R. (2009). Fast and accurate short read alignment with Burrows-Wheeler transform. Bioinformatics *25*, 1754–1760.
64. Li, H., Handsaker, B., Wysoker, A., Fennell, T., Ruan, J., Homer, N., Marth, G., Abecasis, G., and Durbin, R.; 1000 Genome Project Data Processing Subgroup (2009). The Sequence Alignment/Map format and SAMtools. Bioinformatics *25*, 2078–2079.
65. Quinlan, A.R., and Hall, I.M. (2010). BEDTools: a flexible suite of utilities for comparing genomic features. Bioinformatics *26*, 841–842.
66. Kent, W.J., Zweig, A.S., Barber, G., Hinrichs, A.S., and Karolchik, D. (2010). BigWig and BigBed: enabling browsing of large distributed datasets. Bioinformatics *26*, 2204–2207.
67. Zhang, Y., Liu, T., Meyer, C.A., Eeckhoute, J., Johnson, D.S., Bernstein, B.E., Nusbaum, C., Myers, R.M., Brown, M., Li, W., and Liu, X.S. (2008). Model-based analysis of ChIP-Seq (MACS). Genome Biol. *9*, R137.
68. Ewels, P.A., Peltzer, A., Fillinger, S., Patel, H., Alneberg, J., Wilm, A., Garcia, M.U., Di Tommaso, P., and Nahnsen, S. (2020). The nf-core framework for community-curated bioinformatics pipelines. Nat. Biotechnol. *38*, 276–278.
69. Ramírez, F., Ryan, D.P., Grüning, B., Bhardwaj, V., Kilpert, F., Richter, A.S., Heyne, S., Dündar, F., and Manke, T. (2016). deepTools2: a next generation web server for deep-sequencing data analysis. Nucleic Acids Res. *44*, W160–W165.
70. Langmead, B., Trapnell, C., Pop, M., and Salzberg, S.L. (2009). Ultrafast and memory-efficient alignment of short DNA sequences to the human genome. Genome Biol. *10*, R25.
71. Liao, Y., Smyth, G.K., and Shi, W. (2014). featureCounts: an efficient general purpose program for assigning sequence reads to genomic features. Bioinformatics *30*, 923–930.
72. Love, M.I., Huber, W., and Anders, S. (2014). Moderated estimation of fold change and dispersion for RNA-seq data with DESeq2. Genome Biol. *15*, 550.
73. Dobin, A., Davis, C.A., Schlesinger, F., Drenkow, J., Zaleski, C., Jha, S., Batut, P., Chaisson, M., and Gingeras, T.R. (2013). STAR: ultrafast universal RNA-seq aligner. Bioinformatics *29*, 15–21.
74. Pettersen, E.F., Goddard, T.D., Huang, C.C., Meng, E.C., Couch, G.S., Croll, T.I., Morris, J.H., and Ferrin, T.E. (2021). UCSF ChimeraX: Structure visualization for researchers, educators, and developers. Protein Sci. *30*, 70–82.
75. Zhang, S., Cooper, J.A.L., Chong, Y.S., Naveed, A., Mayoh, C., Jayatilleke, N., Liu, T., Amos, S., Kobelke, S., Marshall, A.C., et al. (2023). NONO enhances mRNA processing of super-enhancer-associated GATA2 and HAND2 genes in neuroblastoma. EMBO Rep. *24*, e54977. https://doi.org/10.15252/embr.202254977.
76. Tunyasuvunakool, K., Adler, J., Wu, Z., Green, T., Zielinski, M., Žídek, A., Bridgland, A., Cowie, A., Meyer, C., Laydon, A., et al. (2021). Highly accurate protein structure prediction for the human proteome. Nature *596*, 590–596.

STAR★METHODS

KEY RESOURCES TABLE

REAGENT or RESOURCE	SOURCE	IDENTIFIER
Antibodies		
CBP (D6C5)	Cell Signaling	7389; RRID: AB_2616020
CBP/KAT3A/CREBBP aNTIBODY (c-1)	Santa Cruz (insight)	sc-7300; RRID: AB_626817
Anti-Acetyl-CBP (Lys1535)/p300 (Lys1499)	Cell Signaling	4771; RRID: AB_2262406
Recombinant Anti-Brd4 antibody [EPR5150(2)] (ab128874)	Abcam	ab128874; RRID: AB_11145462
anti-Histone H3 (acetyl K27) antibody	Abcam	ab4729; RRID: AB_2118291
Anti-Histone H4	Abcam	ab10158; RRID: AB_296888
Anti-Histone H3 (acetyl K27)	Abcam	ab4729; RRID: AB_2118291
Anti-Histone H3K27ac	Active Motif	39133; RRID: AB_2561016
Anti-GFP	Abcam	ab290; RRID: AB_2313768
Anti-GFP	Millipore	MAB3580; RRID: AB_94936
Anti-HaloTag® Monoclonal Antibody	Promega	G9211; RRID: AB_2688011
GAPDH	Proteintech	60004–1; RRID: AB_2107436
Alexa Fluor® 488 Goat Anti-Rabbit IgG (H + L) Cross-Adsorbed Secondary Antibody	Invitrogen	A-11008; RRID: AB_143165
Alexa Fluor® 647 AffiniPure Donkey Anti-Rabbit IgG (H + L)	Jackson Laboratories	711-605-152; RRID: AB_2492288
Alexa Fluor® 488 AffiniPure Donkey Anti-Mouse IgG (H + L)	Jackson Laboratories	715-545-150; RRID: AB_2340846
HRP conjugated α-Rabbit IgG	Stratech	211-032-171; RRID: AB_2339149
HRP-conjugated Affinipure Goat Anti-Mouse IgG(H + L)	Proteintech	SA00001-1; RRID: AB_2722565
Bacterial and virus strains		
Stbl3 E.Coli cells	ThermoFisher	C737303
Chemicals, peptides, and recombinant proteins		
Dulbecco's Modified Eagle Medium (DMEM) - high glucose	Fisher	10741574
Fetal Bovine Serum (FBS)	ThermoFisher	10437028
Penicillin Streptomycin Solution 100X	ThermoFisher	11556461
Fetal Bovine Serum, certified, heat inactivated, United States, Tetracycline free	ThermoFisher	10082147
G418	Generon	G810
Hygromycin B	ThermoFisher	10687010
Lipofectamine 3000	ThermoFisher Scientific	L3000008
LipoD293 Version II	TEBU-Bio	SL100668
Lenti-X concentrator	Takara	631232
Polybrene	Merck Millipore	TR-1003-G
Doxycycline hydrochloride	Fisher	CAS 10592-13-9
PFuUltra II fusion HS DNA Polymerase	Agilent	600670
Dimethyl sulfoxide (DMSO)	Sigma	D8418
Applied Biosystems GeneAmp dNTP Blend (10mM)	ThermoFisher	N8080260
NEBuilder HiFi DNA Assembly reaction	NEB	E2621L
NotI-HF	NEB	R3189S

(*Continued on next page*)

Continued

REAGENT or RESOURCE	SOURCE	IDENTIFIER
SbfI	NEB	R3642
T4 DNA ligase	NEB	M0202S
DpnI	NEB	R0176S
T4 polynucleotide kinase (PNK)	NEB	EK0031
NruI-HF	NEB	R3192S
PmlI	NEB	R0532S
Quick Calf Intestinal Phosphatase (CIP)	NEB	M0525S
BamHI-HF	NEB	R3136S
MluI-HF	NEB	R3198S
BssHII	NEB	R0199S
BbsI-HF	NEB	R3539S
QuickExtract solution	Lucigen	QE0905T
T7 Endonuclease 1 (T7E1) enzyme	NEB	M0689S
TRIzol	ThermoFisher	15596018
Turbo DNase	Invitrogen	AM2238
Power SYBR reaction mastermix	ThermoFisher	4368706
Poly-L-lysine hydrobromide	Merck/Sigma	P2636
HaloTag ligand TMR	Promega	G8251
Hoechst 33342 trihydrochloride trihydrate	Invitrogen by ThermoFisher	H3570
Dulbecco's Phosphate-buffered saline	ThermoFisher	14190250
Gibco FluoriBrite	ThermoFisher Scientific	A1896701
Gibco 1M HEPES	ThermoFisher Scientific	15630106
HaloTag Janelia Fluor 549	Promega	GA1110
HaloTag Janelia Fluor 646	Promega	GA1120
1,6 - Hexanediol	Merck	240117
100X Halt protease and phosphatase inhibitor cocktail	Fisher	10085973
RNase A	NEB	T3018
32% Paraformaldehyde solution EM Grade	Electron Microscopy Sciences	15714-S
Bovine Serum Albumin (BSA)	Sigma-Aldrich	A3059-100g
VECTORshield that contained 4,6-diamidino-2-phenylindole (DAPI)	Vector laboratories	H-2000-10
A-485	Selleckchem	S8740
Trichostatin A (TSA)	Stratech, APExBIO	A8183
Dithiothreitol (DTT)	Melford	MB1015-25G
Sodium butyrate	Sigma-Aldrich	303410-100g
Benzonase Nuclease	Sigma-Aldrich	E1014-25KU
Trans-blot turbo mini 0.2 μm nitrocellulose transfer packs	Biorad	1704158
IGEPAL (NP40) CA-630	Sigma	18896-50mL
PMSF	SLS	10837091001
acetyl Coenzyme A sodium salt solution	Sigma	A2056-10MG
recombinant polynucleosomes H3.1	Active Motif	31466
NuPAGE 3–8% Tris-Acetate gel	Invitrogen by thermofisher	EA0378BOX
Tris-Acetate SDS running buffer	Novex by life technologies	LA0041
NuPAGE 4–12% Bis-Tris gel	Invitrogen by thermofisher	NP0335BOX
MOPS SDS running buffer (20X)	Invitrogen by thermofisher	NP0001
16% Formaldehyde Solution (w/v), Methanol-free	ThermoFisher Scientific	28906

(*Continued on next page*)

Continued

REAGENT or RESOURCE	SOURCE	IDENTIFIER
Glycine	Fisher	56-40-6
cOmplete™, Mini, EDTA-free Protease Inhibitor Cocktail	Merck	11836170001
Sodium deoxycholate	Sigma-Aldrich	D6750-100g
N-lauroylsarcosine sodium salt	Sigma	L5777-50g
Proteinase K	NEB	P8107G
Dimethyl sulfoxide (DMSO) anhydrous, 10 × 3mL for resuspending dyes/ligands	Invitrogen	D12345
NuPAGE Sample Reducing Agent (10X)	ThermoFisher	NP0009
NuPAGE LDS Sample Buffer (4X)	ThermoFisher	NP0007
Critical commercial assays		
Neon electroporation system and 100 μL kit	ThermoFisher	MPK10096
Monarch PCR cleanup kit	NEB	T1030L
Qubit dsDNA Broad Range BR kit	ThermoFisher	Q32853
Qubit dsDNA High Sensitivity (HS) kit	ThermoFisher	Q33230
Qubit RNA Broad Range (BR) Assay Kit	ThermoFisher	Q10210
High Capacity cDNA kit	ThermoFisher	4387406
Pierce BCA Protein Assay Kit	ThermoFisher	23227
NEBNext UltraTMII DNA Library Prep Kit for Illumina	NEB	E7645
TapeStation High Sensitivity D1000 ScreenTape	Agilent	5067–5584
CUT&RUN Assay kit	Cell Signaling	86652S
Quant-seq 3′ mRNA-Seq Library Prep kit	Lexogen	191.24
qPCR Add-on Kit	Lexogen	208.96
ChromoTek GFP-Trap® Magnetic Particles M-270	Proteintech	gtd-20
Protein G Dynabeads™	Fisher	10004D
AMPure XP beads	Beckman Coulter	A63880
Deposited data		
The high-throughput sequencing data from this study have been deposited to the GEO database grouped under SuperSeries GSE299618.	https://www.ncbi.nlm.nih.gov/geo/	GEO: GSE299618
ChIP-seq	This study	GEO: GSE268266
CUT&RUN	This study	GEO: GSE299613
RNA-seq	This study	GEO: GSE299614
Experimental models: Cell lines		
HEK293T	ATCC	CRL-3216
GP2-293	Clontech	631458
CBP-Halo HEK293T (clonal)	This paper	Available on request
Doxycycline inducible CBP-WT-GFP HEK293T	This paper	Available on request
Doxycycline inducible CBP-ΔIDR6-GFP HEK293T	This paper	Available on request
Doxycycline inducible CBP-ΔIDR7-GFP HEK293T	This paper	Available on request
Oligonucleotides		
Primers for cloning	IDT	See Table S1
Primers for qPCR	IDT	See Table S1
Synthetic DNA sequences	IDT	See Table S1
CRISPR gene editing	IDT	See Table S1
Recombinant DNA		
pRetroX-pTRE3G	Clontech	Cat#631530
pRetroX-Tet3G	Clontech	Cat#631530

(*Continued on next page*)

Continued

REAGENT or RESOURCE	SOURCE	IDENTIFIER
pVSV-G	Clontech	Cat#631530
pRetroX-TRE3G_CBP-GFP	This study	Addgene #221926
pRetroX-TRE3G_CBPΔIDR6-GFP	This study	Addgene #221927
pRetroX-TRE3G_CBPΔIDR7-GFP	This study	Addgene #221928
pAcGFP-N1_CBP	This study	Addgene #221903
pAcGFP-N1_CBPdIDR1	This study	Addgene #221904
pAcGFP-N1_CBPdIDR3	This study	Addgene #221905
pAcGFP-N1_CBPdIDR4	This study	Addgene #221906
pAcGFP-N1_CBPdIDR6	This study	Addgene #221907
pAcGFP-N1_CBPdIDR7	This study	Addgene #221908
pAcGFP-N1_CBPdCFID	This study	Addgene #221909
pAcGFP-N1_CBPdAL	This study	Addgene #221910
pAcGFP-N1_CBPKTG	This study	Addgene #221911
pAcGFP-N1_CBPdIDR6dAL	This study	Addgene #221912
pAcGFP-N1_CBPdIDR6KTG	This study	Addgene #221913
pAcGFP-N1_CBPdIDR7dAL	This study	Addgene #221914
pAcGFP-N1_CBPdIDR7KTG	This study	Addgene #221915
pAcGFP-N1_CBPdCFIDdAL	This study	Addgene #221916
pAcGFP-N1_CBPdCFIDKTG	This study	Addgene #221917
pHR-mCh-Cry2WT	Gift from Clifford Brangwynne	Addgene #101221
pHR-mCh-Cry2WT-NLS	This study	Addgene #221925
pHR-IDR1-mCh-Cry2WT-NLS	This study	Addgene #221918
pHR-IDR3-mCh-Cry2WT-NLS	This study	Addgene #221919
pHR-IDR4-mCh-Cry2WT-NLS	This study	Addgene #221920
pHR-AL-mCh-Cry2WT-NLS	This study	Addgene #221924
pHR-IDR6-mCh-Cry2WT-NLS	This study	Addgene #221921
pHR-IDR7-mCh-Cry2WT-NLS	This study	Addgene #221922
pHR-CFID-mCh-Cry2WT-NLS	This study	Addgene #221923
pAcGFP-N1_CBPΔIDR6H2-GFP	This study	Addgene #221929
pAcGFP-N1_CBPΔIDR7H1-GFP	This study	Addgene #221930
pAcGFP-N1_CBPIDR6-Shuffle-GFP	This study	Addgene #247245
pAcGFP-N1_CBPIDR7-Shuffle-GFP	This study	Addgene #247246
pSpCas9(BB)-2A-GFP (PX458)	Gift from Feng Zhang	Addgene plasmid # 48138
Software and algorithms		
UCSC CRISPR targets tool	https://genome.ucsc.edu/	N/A
Evaluation tool on the E-CRISP site	https://e-crisp.org/	N/A
Inference of CRISPR Edits (ICE)	Synthego[57]; https://ice.synthego.com/#/	N/A
ImageJ/Fiji	Schindelin et al.[58]	N/A
Stack Registration (StackReg)	Thévenaz et al.[59]	N/A
Zen Blue software	Zeiss	N/A
Zeiss Arivis Pro/Vision4D version 3.4	Zeiss	N/A
R in RStudio	R Core Team[60,61]	N/A
GraphPad prism	Prism (San Diego 2022)	N/A
FastQC v0.11.9	http://www.bioinformatics.babraham.ac.uk/projects/fastqc/	N/A
Cutadapt v3.4	Martin[62]	N/A
Trim Galore	https://www.bioinformatics.babraham.ac.uk/projects/trim_galore/	N/A
Burrows-Wheeler Alignment, v0.7.17-r1188	Li and Durbin[63]	N/A
Picard v2.27.4	https://broadinstitute.github.io/picard/	N/A

(*Continued on next page*)

Continued

REAGENT or RESOURCE	SOURCE	IDENTIFIER
SAMTools v1.15.1	Li et al.[64]	N/A
Bedtools v2.30.0	Quinlan and Hall[65]	N/A
UCSC utilities, bedGraphToBigWig v377	Kent et al.[66]	N/A
MACS2 v2.2.7.1	Zhang et al.[67]	N/A
Nextflow ChIP-seq pipeline v2.00	Ewels et al.[68]	N/A
Bedtools v2.31.0	Favorov et al.[45]	N/A
DeepTools v3.5.5 (ChIP-Seq), v3.5.3 (CUT&RUN)	Ramirez et al.[69]	N/A
bowtie2 v2.5.4	Langmead et al.[70]	N/A
featureCounts v2.0.6	Liao et al.[71]	N/A
DEseq2 v1.40.2	Love et al.[72]	N/A
MACS3 v3.0.0b1	Zhang et al.[67]	N/A
STAR v2.7.6	Dobin et al.[73]	N/A
DISOPRED3	Jones and Cozzetto[24]	N/A
PONDR, VSL2 predictor	Xue et al.[25]	N/A
localCIDER	Holehouse et al.[35]	N/A
PLAAC analysis	Lancaster et al.[37]	N/A
GOOSE	Hunter et al.[38]	N/A
AlphaFold version 2.3.2	Jumper et al.[26]	N/A
UCSF ChimeraX	Pettersen et al.[74]	N/A
Other		
FACSMelody cell sorter	BD Biosciences	N/A
Quantstudio 12K Flex	Applied Biosystems	N/A
Illumina NovaSeq 6000 platform	Novogene	N/A

EXPERIMENTAL MODEL AND STUDY PARTICIPANT DETAILS

Cell culture

Human embryonic kidney cells (female) cells stably expressing the SV40 large T antigen (HEK293T) were obtained from ATCC. GP2-293 for retroviral packaging were obtained from Clontech. All HEK293 derived lines were cultured in complete DMEM (10% FBS, 1% Penicillin-Streptomycin (Gibco)) and grown in 5% CO_2 at 37°C. HEK293T cells containing stable doxycycline inducible CBP-GFP, were cultured in complete DMEM (10% Tetracycline free FBS, 1% Penicillin-Streptomycin) including 2 mg/mL G418 (Generon) and 50 μg/mL hygromycin (ThermoFisher). Cell lines were not authenticated. All cell lines were screened every three months for mycoplasma infection. Only female cells (HEK293T) were used in this study as they are a standard model for high-efficiency transfection and the biological processes being studied are not known to be sex-specific.

METHOD DETAILS

Cell culture and maintenance

Transient transfections

Transient transfections were done using either Lipofectamine 3000 (ThermoFisher Scientific) or LipoD293 (TEBU-Bio). Manufacturers' recommended protocol was followed for 6-well dishes with the following details: 1.5 μg of DNA was transfected per well and 7.5 μL of Lipofectamine 3000 reagent was used per well. For LipoD293 (TEBU-Bio), the manufacturers protocol for 6-well 35-mm dishes was followed using: 1 μg of DNA and 3 μL of LipoD293 per well.

Retroviral transduction

Lentiviral transduction of CBP-GFP was done using the pRetroX Tet-On^R 3G inducible expression system (Clontech). CBP_{WT}-GFP, $CBP_{\Delta IDR6}$-GFP, and $CBP_{\Delta IDR7}$-GFP were cloned into the pRetroX-pTRE3G vector for lentiviral transduction. To generate lentiviral particles, 2 μg of CBP-pRetroX-pTRE3G constructs or pRetroX-Tet3G were co-transfected with 2 μg of the envelope pVSV-G plasmid into GP2-293 cells using lipofectamine 3000 (ThermoFisher). After 48 h, with 1 media change after 24 h, the viral supernatant was collected and concentrated using Lenti-X concentrator (Takara) following manufacturers instructions. To generate polyclonal pRetroX-Tet3G HEK293T cells, 8 μg/mL polybrene (Merck Millipore) was added to the concentrated virus and used to infect HEK293T cells. Infected cells were selected using G418 (Generon) at a concentration of 8 mg/mL for 1 week. To generate CBP-pRetroX-pTRE3G cells, polyclonal pRetroX-Tet3G HEK293T cells were transduced with viral particles and 8 μg/mL polybrene,

then selected using 8 mg/mL of G418 and 125 μg/mL hygromycin (ThermoFisher) for 1 week. Clonal cell lines were generated by inducing expression of CBP-GFP with 2000 ng/mL of doxycycline for 48 h before fluorescence-activated cell sorting (FACS) based on the GFP signal, using a FACSMelody Cell Sorter (BD Biosciences) at the University of Sheffield Flow Cytometry Core Facility. Clonal lines were cultured in the background of 2 mg/mL G418 and 50 μg/mL hygromycin (ThermoFisher).

Doxycycline induction of CBP expression

For doxycycline validation experiments, HEK293T cells were plated in 10 cm dishes (Sarstedt) for western blot or 35-mm glass bottom dishes (Ibidi) for imaging. 24 h post-plating the media was changed to media containing the predetermined concentration of doxycycline calculated to ensure induction of CBP-GFP but not increase overall CBP expression levels (Figures S4K and S4L), 2 mg/mL G418 and 50 μg/mL hygromycin.

Molecular biology and cloning

All PCR reactions were completed using a 50 μL reaction containing: 0.5 μL PFuUltra II fusion HS DNA Polymerase (Agilent), 1% PFu Ultra reaction buffer, 5% dimethyl sulfoxide (DMSO, Sigma), 200 mM dNTP mix, 0.2 μM forward and reverse primer, and template DNA. DNA was initially denatured at 95°C with an extension temperature of 68°C for DNA less than 10 kb, and 72°C for DNA greater than 10 kb, with 35 extension cycles unless otherwise stated. To confirm correct assembly and presence of mutations, all plasmids were checked by Sanger sequencing and most were checked by Whole plasmid sequencing (Eurofins). All Constructs have been made available through Addgene (https://www.addgene.org/).

Full-length human CBP (CBP_{WT})

To generate human CBP_{WT} (transcript variant 1, NCBI Reference: NM_004380.3) tagged with a C-terminal GFP for overexpression experiments (CBP_{WT}-GFP), *Homo sapiens* CBP transcript variant 2 (NCBI Reference NM_001079846.1, Sino Biological HG17295-UT) was cloned in-frame into pAcGFP-N1 (Clontech) using NEBuilder HiFi DNA Assembly reaction protocol (NEB). CBP was amplified using primers: *Fwd: Human CBP_fwd, Rev: Human CBP_rev* and pAcGFP-N1 was amplified using primers: *Fwd: pAcGFP-N1_fwd, Rev: pAcGFP-N1_rev*; (For primer sequences see Table S1). Assembled constructs were checked by Sanger sequencing (Eurofins). To convert transcript variant 2 to transcript variant 1, the missing sequence comprising exon 5 was ordered as a custom-synthesized DNA from IDT and inserted into CBP-pAcGFP-N1 using the NEB HiFi assembly. CBP exon 5 was amplified using primers: *CBP missing Exon_fwd, CBP missing Exon_rev*. CBP-pAcGFP-N1 was amplified using primers: *Fwd: GFP-CBP_fwd, Rev: GFP-CBP_rev*. Fully assembled CBP_{WT}-GFP was sequenced by Sanger sequencing using sequential primers at 900bp intervals and confirmed using Whole Plasmid Sequencing (Eurofins) to check for correct assembly.

CBP-IDRs for optoDroplet

The optoDroplet construct pHR-mCh-Cry2WT was a gift from Clifford Brangwynne (Addgene plasmid #101221).[32] To target the optoDroplet construct to the nucleus we used custom synthesized DNA (gBlock, IDT) encoding the SV40 nuclear localization signal (NLS) to generate pHR-mCh-Cry2WT-NLS. The SV40 NLS was amplified by PCR using primers: *Fwd: SV40_NLS_NotIRD_fwd, Rev: SV40_NLS_SbfIRD_rev*, to introduce restriction sites for NotI and SbfI. Following restriction digestion with NotI-HF and SbfI (NEB), pHR-mCh-Cry2WT and the synthesized NLS were ligated using T4 DNA ligase (NEB) and the construct was checked by Sanger sequencing. CBP-IDRs were cloned into pHR-mCh-Cry2WT-NLS construct using the NEB HiFi DNA assembly protocol. pHR-mCh-Cry2WT-NLS was amplified using primers: *Fwd: pHR-mCh-Cry2WT-NLS_fwd, Rev: pHR-mCh-Cry2WT-NLS_rev*. CBP-IDRs were amplified from CBP_{WT}-GFP using IDR-specific primers (Table S1). All constructs were checked using Sanger sequencing.

$CBP_{\Delta IDR}$-GFP deletion mutants

To generate $CBP_{\Delta IDR}$ mutants, primers were designed to amplify CBP_{WT}-GFP in reverse directions to delete residues comprising the identified CBP-IDRs (Table S1). Amplified PCR products were digested using DpnI (NEB), the ends of the PCR fragments were then phosphorylated using T4 polynucleotide kinase (PNK, NEB) before undergoing ligation using T4 DNA ligase (NEB). Constructs were sequenced by Sanger sequencing to check the IDRs had been correctly removed from the construct.

Autoregulatory loop (CBP_{AL}) mutants

Two mutants of the Autoinhibitory Loop (CBP_{AL}, $CBP_{1558\text{-}1607}$) were designed. Firstly, CBP_{KTG} contained the AL with all lysines mutated to glycine (K1564G, K1565G, K1583G, K1586G, K1587G, K1588G, K1591G, K1592G, K1595G, K1597G, K1605G, K1606G, and K1607G). Secondly, in $CBP_{\Delta AL}$ the AL was replaced with a glycine/serine linker (sequence GSAGSAAGSGQF) to maintain correct folding.[33] $CBP_{4322\text{-}5818}$ - which are flanked by unique restriction sites for NruI and PmlI - were synthesized as gBlocks (IDT) containing the mutant AL sequences (Table S1). The synthesized gBlocks and CBP-pAcGFP-N1 constructs (CBP-GFP for single mutants; $CBP_{\Delta IDR6}$-GFP, $CBP_{\Delta IDR7}$-GFP, and $CBP_{\Delta CFID}$-GFP for double mutants) were digested using NruI-HF and PmlI (NEB). The digested constructs were dephosphorylated using Quick Calf Intestinal Phosphatase (CIP, NEB), before the inserts and vectors were assembled using T4 DNA ligase (NEB). The assembled constructs were checked by Sanger sequencing.

Doxycycline-inducible CBP-GFP

CBP-GFP, $CBP_{\Delta IDR6}$-GFP, and $CBP_{\Delta IDR7}$-GFP were sub-cloned into a modified pRetroX-pTRE3G plasmid (Clontech) containing a hygromycin resistance cassette using BamHI-HF and NotI-HF (NEB) restriction enzymes. The fragments were annealed using T4 DNA ligase (NEB) before sequencing to check for correct insertion and subsequently by whole plasmid sequencing.

$CBP_{\Delta IDR6H2}$-GFP and cloning $CBP_{\Delta IDR7H1}$-GFP

To delete predicted a-helices in CBP_{IDR6} and CBP_{IDR7}, DNA sequences were synthesized containing CBP 5332–7674 which resides within the N-terminal GFP tag, and spans two unique endogenous restriction sites for MluI-HF and BssHII (GeneArt, ThermoFisher).

Synthesized sequences contained deletions of $CBP_{1951-1978}$ ($CBP_{\Delta IDR6H2}$-GFP) and $CBP_{2187-2216}$ ($CBP_{\Delta IDR7H1}$-GFP). CBP_{WT}-GFP and synthesized sequences were digested with MluI-HF and BssHII (NEB) and purified by agarose gel extraction. The digested CBP_{WT}-GFP vector was dephosphorylated using Quick Calf Intestinal Phosphatase (CIP, NEB) before assembly using T4 DNA ligase (NEB). Correct insertion was checked by Sanger sequencing.

$CBP_{IDR6\text{-}shuffle}$-GFP and cloning $CBP_{\Delta IDR7\text{-}shuffle}$-GFP

DNA sequences were synthesized of CBP_{IDR6} and CBP_{IDR7} where the overall sequence composition was maintained but the sequence was randomly shuffled to disrupt the sequence patterning. Design of the shuffled sequences was performed using GOOSE[38] to randomize the input sequence amino acid sequence. DNA coding for the shuffled sequences was designed and codon optimized for expression in *H. sapiens* (GeneArt, ThermoFisher). The synthesized DNA contained two unique restriction sites for MluI-HF and BssHII, cloning was performed as described for $CBP_{\Delta IDR6H2}$-GFP and Cloning $CBP_{\Delta IDR7H1}$-GFP.

Cloning of gRNA plasmids

Designed gRNAs (Table S1) were cloned into pSpCas9(BB)-2A-GFP (PX458). PX458 was a gift from Feng Zhang (Addgene plasmid # 48138). 100 μM forward and reverse oligo pairs were combined with T4 polynucleotide kinase (PNK) (NEB) and 10X T4 ligation buffer (NEB) containing essential ATP. For annealing, reactions were heated to 37°C for 30 min, followed by 95°C for a further 5 min and then cooled to 25°C at a ramp rate of -5°C per minute. Annealed gRNAs were then diluted 1:100 in sterile H_2O in preparation for the ligation reaction.

pX458 plasmid was digested with BbsI-HF (NEB) DNA and annealed gRNA oligos were ligated using T4 DNA ligase (NEB). Constructs were validated using Sanger sequencing.

Construction of stably integrated CBP-Halotag cell lines

gRNA design

Single guide RNAs (sgRNAs) targeting the C terminus of CBP were designed using the UCSC CRISPR targets tool (https://genome.ucsc.edu/). After selection in UCSC, crRNAs were further evaluated using the Evaluation tool on the E-CRISP site (https://e-crisp.org/). Plasmids encoding CBP-targeting sgRNAs were transfected into HEK293T cells using the Neon electroporation system and 100 μL kit (ThermoFisher), at 1100V, 20 ms pulse width and 2 pulses. After 48 h, genomic DNA was extracted using QuickExtract solution (Lucigen) according to the manufacturer's instructions and PCR of CBP C-terminal region was carried out using primers *CBP_C-T_fwd1/2, CBP_C-T_rvs* (Table S1).

gRNA validation

PCR products amplifying the C-terminal region of CBP in both edited and unedited cells were cleaned up using the Monarch PCR cleanup kit (NEB). DNA concentrations were measured using the Qubit dsDNA BR kit (ThermoFisher) according to the manufacturer's instructions. 10X NEB buffer 2 (NEB) was added to 200 ng DNA and PCR products were denatured to single strands by heating at 95°C for 5 min. DNA strands were then hybridized by decreasing temperature from 95°C to 85°C at a ramp rate of -2°C/s, then from 85°C to 25°C at a ramp rate of −0.1°C/s. T7 Endonuclease 1 (T7E1) enzyme (NEB) was added and incubated at 37°C for 15 min, followed by quenching with 0.25 M EDTA. The total reaction volume was run on a 1% agarose gel. To analyze Sanger sequencing data of CRISPR edited DNA sequences, .ab1 files of CBP C-terminal PCR products were uploaded to the Inference of CRISPR Edits (ICE, Synthego) tool.

Generation of clonal CBP-Halo HEK293T cell lines

Validated plasmids encoding CBP gRNA and custom synthesized CBP HDR template plasmid (Table S1, ThermoFisher) were co-transfected into HEK293T cells using the Neon electroporation system and 100 μL kit (ThermoFisher) at 1100V, 20 ms pulse width and 2 pulses. After 48 h, single cell sorting was performed using a FACSMelody cell sorter (BD Biosciences) into 96-well plates. Clones were allowed to grow until confluent and then screened PCR genotyping for successful integration of the Halotag using primers *CBP_C-T_fwd1/2, CBP_C-T_rvs* (Table S1). We performed sufficient screening to identify heterozygous clones. However, we cannot eliminate the possibility that the C-terminal HaloTag caused detrimental effects for CBP function that resulted in no homozygotes being obtained.

qPCR

Total RNA was extracted from WT and CBP-HaloTag HEK293T cells, using TRIzol (ThermoFisher) and treated with Turbo DNase (Invitrogen) to remove genomic DNA, then purified using phenol/chloroform and ethanol precipitation. Reverse Transcription was performed using the High Capacity cDNA kit (ThermoFisher) and qPCR was carried out using Power SYBR reaction mastermix (ThermoFisher) and a Quantstudio 12K Flex (ThermoFisher). A mean Ct was calculated using each triplicate reaction and normalized to 18S rRNA expression.

Imaging

Live-cell imaging of CBP-HaloTag

HEK293T cells containing endogenous CBP-HaloTag were seeded at 400,000 cells/well on 35 mm glass bottom dishes that had been coated in 20 μg/mL of poly-L-lysine (PLL, Merck) diluted in sterile dH_2O for 1 h at 37°C, before washing twice in sterile dH_2O. After 48 h, cells were labeled with HaloTag ligand TMR (Promega) at a concentration of 50 nM for 15 min at 37°C in the dark. Cells were left for a further 2 h before staining with Hoechst 33342 (Fisher) in DPBS as described in a previous section, before washing in DPBS and storing in imaging media (FluoroBright DMEM (Fisher) supplemented with a final concentration of 20 nM Gibco

HEPES (ThermoFisher Scientific)) immediately prior to imaging. Cells were imaged using the Nikon W1 spinning disc confocal microscope equipped with a temperature stage set to 37°C. Images were taken using the 100X oil immersion lens (NA 1.45), using the 405 nm laser to image Hoechst using 45% laser power with a 100 ms exposure, TMR was visualized using the 514 nm laser using 60% laser power with an exposure of 300 ms. Images were taken every 500 ms in the absence of binning. Captured images and videos were processed ImageJ/Fiji.[57]

FRAP of CBP-HaloTag

CBP-HaloTag cells were plated on PLL coated 35-mm dishes and labeled with Janelia Fluor® 549 (JF549, Promega) at a concentration of 50 nM for 15 min. Cells were subsequently washed twice in DPBS and placed in imaging media for a 15-min recovery. Cells were imaged using a custom built iLas TIRF/FRAP single-molecule scanning microscope by Cairn. Puncta were imaged using 561 nm laser with 200 ms exposure at 10% laser power, on the 100% oil objective. ROIs were drawn with a diameter of 10 to mark where the lasers should target, this could be multiple puncta per field of view. FRAP settings are as follows: 10 repetitions using the 561 nm laser line of weight 2 on 3% laser power. A time course was taken with the following pattern: 15 time points with a 500 ms delay prior to FRAP which was performed as described above, followed by 60 time points with a 500 ms delay and 30 time points with a 2 s delay. Images were quantified and processed in ImageJ/Fiji. FRAP curves were calculated for 7 condensates where the bleached area did not diffuse away from the focal plane during the recovery period.

Imaging of transfected CBP-HaloTag with CBP-GFP, CBP$_{\Delta IDR6}$-GFP, CBP$_{\Delta IDR7}$-GFP

Endogenous CBP-HaloTag cells were seeded at 250,000 cells/well on PLL coated glass bottom 35-mm dishes and transfected after 24 h with CBP-GFP, CBP$_{\Delta IDR6}$-GFP, CBP$_{\Delta IDR7}$-GFP using LipoD293, as has been previously described. Cells were labeled with Janelia Fluor® 646 (JF646, Promega) at a final concentration of 2 nM for 15 min before washing in DPBS and imaging in imaging media. 35 mm dishes were labeled sequentially, immediately before imaging.

Imaging using custom built iLas TIRF/FRAP single-molecule scanning microscope by Cairn

4-color control images were also taken where the HaloTag had not been labeled, to check for bleed-through of overexpressed constructs. In this case, the media was changed to imaging media and imaged using laser lines 405 nm, 488 nm, 532 nm and 637 nm, with an exposure time of 200 ms using 10% laser power. A 4-color control was also taken with CBP-HaloTag labeled with JF646 and no overexpression, for this all laser lines used the same conditions as before except the 637 nm laser had a power of 80% to visualize the endogenous protein. For colocalization experiments, 2 color multidimensional images were captured using the 488 nm laser with 10% laser power and a 200 ms exposure to visualize GFP tagged constructs, and 637 nm laser with 80% laser power and 200 ms exposure to view endogenously tagged HaloTag. Images were processed in ImageJ/Fiji.

Imaging using Zeiss Lattice Lightsheet 7

3D images of CBP-HaloTag and overexpressed CBP-GFP, CBP$_{\Delta IDR6}$-GFP, CBP$_{\Delta IDR7}$-GFP were taken using the Zeiss Lattice Lightsheet 7, using the Sinc3 30 x 1000 lightsheet with a calibrated magnification of 50. The system was calibrated following manufacturers guidelines. 488 nm laser line was used to image overexpressed GFP tagged constructs at 40% laser power using 50 ms exposure, the endogenous CBP-HaloTag was imaged using the 638 nm laser line using 80% laser power with a 100 ms exposure. Zen Blue software was used to deskew the dataset and for representative images channel alignment was performed using default settings, where the CBP-HaloTag (638 nm images) were used for reference. Images were then pre-processed in ImageJ/Fiji, before quantification using Arivis Vision4D version 3.4.

Imaging of doxycycline-inducible clones

For imaging cells were seeded at a concentration of 250,00 cells/well on PLL coated 35-mm dishes and doxycycline induced for 48 h. Imaging was performed in imaging media using the Nikon W1 spinning disc confocal microscope, using the 100× oil objective. Laser lines 405 nm and 488 nm were used to image the Hoechst 33342 (Fisher) and therefore the nuclei, and GFP expression respectively. The 405 nm laser was set with a 100 ms exposure with 60% laser power, and the 488 nm laser was set with 300 ms exposure time and 60% laser power. For quantification Z-stacks were taken to capture the whole volume of the nuclei in 0.5 μm increments, these were further processed in ImageJ/Fiji. For the plus doxycycline conditions, imaging media was supplemented with the appropriate concentration of doxycycline.

optoDroplet

35-mm glass bottomed dishes (Ibidi) were coated in PLL for 1 h at 37°C before being washed twice with dH_2O and seeded with HEK293T cells at a concentration of 200,000 cells/well. 24 h post-plating the cells were transfected using LipoD293(SignaGen Laboratories), following manufacturer's guidelines for 35 mm dishes. After 24 h the media was changed into complete DMEM (10% FBS, 1% Pen/Strep). After a further 24 h, prior to imaging the media was changed into FluoroBright DMEM (Fisher) with a final concentration of 20 mM HEPES (ThermoFisher).

For IDR1, IDR3, IDR4, AL, IDR6, IDR7 and the CFID the live cell imaging was performed on Nikon A1 confocal using the 60× oil immersion objective (NA 1.4), equipped with a humidified temperature stage set to 37°C. For the IDR2 and IDR5 live cell imaging was performed on the Nikon W1 spinning disc confocal microscope, using a temperature stage set to 37°C and the 100× oil objective lens. In both cases, two laser wavelengths were used to induce global activation of the optoDroplet system; 488 nm to induce the dimerization of the Cry2 and 560 nm to image mCherry. An image was captured for the mCherry every 8 s, with subsequent activation of the mCherry for the same time. Time courses were taken for each construct, for a period of up to 3 min 3 time courses were taken per construct per biological replicate, with a total of 3 biological replicates being taken.

Fluorescence recovery after photobleaching (FRAP) in transfected cells

For FRAP experiments, 250,000 cells/well of HEK293T cells were plated in 35 mm dishes and transfected using LipoD293 as was described for the optoDroplet live cell imaging. 24-h post transfection the media was removed and the cells were washed in DPBS before leaving the cells in imaging media. Imaging was performed using a custom built iLas TIRF/FRAP single-molecule scanning microscope by Cairn, using an 100× oil immersion objective. Puncta was visualized using the 488 nm laser set to 5% laser power with a 100 ms exposure. A circular ROI with dimensions of 4.4 × 4.4 μm was drawn over the puncta to be photobleached; there may be multiple regions within each field of view. Photobleaching was performed using the 488 nm laser, with 10% laser power, using 5 repetitions with a thickness of 5. 10 images were taken prior to FRAP, followed by 700 frames being collected after, with a frame interval of 0.387 s.

1,6 - Hexanediol treatment

Cells were plated and transfected as previously described for FRAP in transfected cells. Images were captured using the Nikon W1 spinning disc confocal microscope using the 100× oil immersion objective. Images were taken using the 488 nm laser with a 200 ms exposure time on 20% laser power. A 10% solution of 1,6 - Hexanediol (Merck) was diluted from a 50% stock in warm imaging media. Time courses were taken of the constructs over a 3 min period, imaging every 500 ms. Without pausing imaging, after 30 s 1 mL of 10% 1,6 - Hexanediol was added dropwise to the 35 mm dish that contained 1 mL of imaging media for a final concentration of 5% 1,6 - Hexanediol. Imaging continued until the end of the time course. Image quantification and processing was performed in ImageJ/Fiji.

RNase treatment

Cells were plated and transfected in 35 mm glass bottom plates as described above. On the day of imaging, the media was removed and replaced with FluoroBrite media and images were collected of the untreated cells. The cells were then RNase treated[75] as follows: firstly the cells were washed with PBS and reaction buffer (20 mM Tris pH 7.5, 5 mM $MgCl_2$, 0.5 mM EGTA, 1x protease inhibitor cocktail) before being permeated with 0.1% Triton X-100 for 5 min. A second round of washes was then applied before 20 min incubation with 0.2 mg/mL final RNase A (NEB), diluted in the nuclease buffer (5 mM $MgCl_2$ in PBS) to a final concentration of 100 μg/mL. After treatment the RNase solution was removed and replaced with imaging media. Images were subsequently collected of the treated cells. Imaging was performed using the Nikon W1 spinning disc confocal microscope, using the 100× oil objective. The 488 nm laser line was used to image GFP expression. For quantification Z-stacks were taken to capture the whole volume of the nuclei in 0.5 μm increments, these were further processed in ImageJ.

Immunofluorescence and fixed cell imaging

Circular coverslips (Ibidi) were acid washed in 0.25% acetic acid before washing and storing in 100% ethanol. Coverslips were coated in poly-L-lysine (PLL, Merck) for 1 h at 37°C before washing twice in sterile dH_2O. HEK293T cells were grown in 6-well plates at a concentration of 200,000 cells/well containing two coverslips per well for 48 h before fixing. If the cells were transfected, transfection was performed 24 h after plating using Lipofectamine 3000 transfection reagent (ThermoFisher) or LipoD293 (TEBU-Bio) following manufacturers instructions. Cells were washed in DPBS twice before fixing in 2% paraformaldehyde (PFA) for 30 min at room temperature in the dark, before being washed 3 times in DPBS.

For immunofluorescence, coverslips were blocked using a blocking buffer (5% Bovine serum albumin (BSA) with 0.2% Triton in PBS) for 1 h at 37°C. Primary antibodies (for full list of antibodies see Table S2) were prepared in a blocking buffer and incubated at 37°C for 1 h. After washing 3 times in PBS, secondary antibodies were diluted in the blocking buffer and incubated for 37°C for 1 h. After fixing, coverslips were mounted onto slides (VWR, 631–1554) using VECTORshield that contained 4,6-diamidino-2-phenylindole (DAPI) (Vector laboratories, H-2000-10). Fixed slides were stored at 4°C.

Imaging work was performed at the Wolfson Light Microscopy Facility, the majority of imaging was done using the Nikon A1 confocal microscope. All fixed cell imaging was performed using the 60× oil immersion objective (NA 1.4). The microscope has 4 laser wavelengths, typically only 3 of the 4 were used (these include, 405 nm for DAPI, 488 nm for GFP, 562 nm for mCherry and 642 nm for Alexa Fluor 647). Z-stacks were taken every 0.5 μm to cover the depth of the nuclei; a minimum of 3 fields of view were imaged per construct over 2 coverslips, per biological replicate. For CBP deletion mutants $CBP_{\Delta IDR2}$ and $CBP_{\Delta IDR5}$ images were captured on the Nikon W1 spinning disc confocal microscope, using the 100× oil objective and the 488 nm laser line. Z-stacks were taken, and data collected, as described above.

A-485 treatment

Cells were cultured in 6-well plates, containing PLL-treated circular coverslips as described above. HEK293T cells were transfected with LipoD293 (TEBU-Bio) after 24 h following manufacturers instructions. For 36 h A-485 treatment, media was removed after 8-h of transfection and replaced with media supplemented with A-485 to a final concentration of 5 μM, or with media containing DMSO as a negative control. The cells were treated for 36 h before fixing with 2% paraformaldehyde and mounted on slides using VECTORshield containing DAPI as described above.

For the A-485 concentration experiments, cells were transfected after 24 h of culture, and treated 24 h after transfection. Media was replaced either 2 h before fixing or 1 h before fixing with media containing A-485 at concentrations of 1 μM, 5 μM or 10 μM. A DMSO control was performed at each time point. After treatment cells were fixed as described above. Imaging was performed using the Nikon W1 spinning disc confocal microscope, using the 100× oil objective. Laser lines 405 nm and 488 nm were used

to image the DAPI and therefore the nuclei, and GFP expression respectively. For quantification Z-stacks were taken to capture the whole volume of the nuclei in 0.5 μm increments, these were further processed in ImageJ/Fiji.

TSA treatment

Cells were cultured in 6-well plates, containing PLL-treated circular coverslips as described above. HEK293T cells were transfected with LipoD293 (TEBU-Bio) after 24 h following manufacturers instructions. After ~36 h cells were treated with Trichostatin A (TSA, Stratech) at a final concentration of 500 nM for 90 min. After 90 min the cells were fixed and imaged as described above for A-485 treatment.

Western blotting

For western blotting HEK293T cells were plated in 10 cm dishes (Sarstedt), and induced or treated as described in the imaging section. Cells were harvested and after washing twice in PBS the pellet was lysed in RIPA buffer (50 mM Tris-HCl pH 8 stored at 4°C, 100 mM NaCl, 2 mM $MgCl_2$, 1% Triton X-100, 0.1% Sodium deoxycholate, 0.1% Sodium Dodecyl Sulfate (SDS)) supplemented with 1 mM Dithiothreitol (DTT), 1X Halt protease inhibitor cocktail, 10 mM sodium butyrate and 500 U/μL benzonase. 25–50 μg of overall protein containing sample buffer and reducing buffer was loaded onto either a 3–8% Tris-Acetate gel (Thermo Fisher Scientific) using Tris Acetate running buffer (Life Technologies) for large proteins such as CBP, or 4–12% Bis-Tris gel with MOPS running buffer for visualizing small things such as H3K27ac. Gel was transferred onto a membrane using *trans*-blot turbo mini 0.2 μm nitrocellulose transfer packs (Biorad) before blocking and probing for CBP, GFP, acetylated CBP 1535, H3K27ac and GAPDH (for full list of antibodies see Table S2). Western blots were imaged using G:box (Syngene) gel imager. Images were processed using ImageJ/Fiji and assembled using Adobe Illustrator. Western blots were quantified using ImageJ/Fiji.

Histone acetyltransferase assay

Expression of CBP_{WT}-GFP, $CBP_{\Delta IDR6}$-GFP, $CBP_{\Delta IDR7}$-GFP was induced in the respective cell lines by 48 h treatment with previously determined doxycycline concentrations to ensure equal expression levels (Figures 4M, S4K, and S4L). Cells were harvested immediately after doxycycline treatment for cell lysis. Cells were washed with PBS and resuspended in NET buffer (50 mM Tris-HCl, 150 mM NaCl, 2 mM MgCl2, 2 mM CaCl2, 2 mM ZnCl2) supplemented with 0.1% NP40, 10mM sodium butyrate and Halt Protease and Phosphatase Inhibitor Cocktail. Lysed cells were incubated with benzonase (1kU) at 37°C for 30 min, followed by centrifugation at 4°C to obtain the cell lysate. To immunoprecipitate CBP-GFP, 500 μg - 1 mg cell lysate was incubated with either 25 μL ChromoTek GFP-Trap Magnetic Particles M-270 or 50 μL Protein G Dynabeads. After recovery, beads were resuspended in 500 μL of wash buffer (NET buffer supplemented with 10mM sodium butyrate and 0.05% NP-40). 300 μL of the bead suspension was retained for a western blot to confirm successful immunoprecipitation of the GFP-tagged protein. The remaining 200 μL was used for the *in vitro* HAT assay.

Beads were resuspended in HAT buffer (250 mM Tris-HCl, 25% glycerol, 0.5 mM EDTA, 250 mM KCl) supplemented with 0.1M DTT, 10 mM PMSF, 1M sodium butyrate, 1 mM acetyl CoA and 0.55 μg/mL recombinant polynucleosomes (H3.1; Active Motif) and the reaction mixture was incubated for 30 min at 30°C. After incubation, loading dye and reducing agent were added before boiling the beads. 50 μg of overall protein was loaded onto either a 3–8% Tris-Acetate gel with Tris Acetate running buffer (to visualize CBP) or a 4–12% Bis-Tris gel with MOPS running buffer (to visualize H3K27ac).

Chromatin immunoprecipitation (CHIP)

For ChIP experiments, Dox inducible cells were plated in 10 cm dishes, 2 plates per construct. Cells were induced with concentrations of Dox that were identified using western blot as inducing CBP-GFP without altering overall CBP expression levels (Figures 4M, S4K, and S4L). After 48 h, cells were crosslinked at room temperature for 10 min using formaldehyde (1.1% final). Crosslinking was quenched using 2.5 M Glycine (Melford, 125 mM final) incubating for 5 min at room temperature. Cells were harvested by cell scraping in PBS, and pelleted by centrifugation at 200 rcf for 5 min. Cell lysis was performed in ChIP lysis buffer 1 (50 mM HEPES-KOH (Sigma), pH 7.5 140 mM NaCl, 1 mM EDTA, 10% Glycerol, 0.5% NP40, 0.25% Triton X-100, Complete protease inhibitor cocktail (Roche)) by rotating at 4°C for 5 min. Nuclei were pelleted by centrifugation at 1500 rcf for 5 min, re-suspended in ChIP Buffer 2 (10 mM Tris-HCl pH 8.0, 200 mM NaCl, 1 mM EDTA, 0.5 mM EGTA (Sigma), Complete protease inhibitor cocktail) and incubated at room temperature on a rotator for 10 min. Nuclei were pelleted by centrifugation at 1500 rcf for 5 min and re-suspended in ChIP lysis buffer 3 (10 mM Tris-HCl pH 8.0, 200 mM NaCl, 1 mM EDTA, 0.5 mM EGTA, 0.1% Na-deoxycholate, 0.5% N-lauroylsarcosine (Sigma), Complete protease inhibitor cocktail) for shearing. Chromatin was sheared to 150–300 bp fragments, using the Bioruptor Pico (Diagenode), samples were sonicated for 12 cycles of 30 s on, 30 s off pulse sonication. Lysates were cleared by centrifugation at 20,000xg for 20 min. Concentrations of lysates was determined by BCA assay (ThermoFisher), IP's were done with 900 μg of sheared protein in a total of 300 μL with ChIP IP buffer (10 mM Tris-HCl pH 8.0, 600 mM NaCl, 1 mM EDTA, 3% Triton X-100, Complete protease inhibitor cocktail), input reactions were made for each sample with 90 μg of protein in 50 μL of ChIP IP buffer. Immunoprecipitations were performed by incubating with 4 μg of antibody overnight with rotation at 4°C. Immunocomplexes were recovered by adding blocked Protein G Dynabeads and incubated for 90 min at 4°C with rotation. Beads were washed 5 times in ChIP wash buffer (50 mM HEPES-KOH pH 7.5, 500 mM LiCl, 1 mM EDTA, 1% NP40, 0.7% Na-deoxycholate, 0.1% N-lauroylsarcosine) and 1x in ChIP final wash buffer (10 mM Tris-HCl pH 8.0, 1 mM EDTA, 50 mM NaCl). Sample was eluted by incubation at 65°C for 30 min in ChIP elution buffer (50 mM Tris-HCl pH 8.0, 200 mM NaCl, 10 mM EDTA, 1% SDS) with rotation in a thermomixer at 900 rpm. Cross-linking was reversed by incubation at 65°C overnight. Immunoprecipitated DNA was treated with

RNase A (0.2 mg/mL final), supplemented with 4 mM $CaCl_2$ for 2 h at 37°C, then Proteinase K (0.2 mg/mL final) for 2 h at 55°C. DNA was then purified by phenol:chloroform extraction and ethanol precipitation and resuspended in 1x TE buffer.

ChIP-seq library preparation

For ChIP-seq, samples were prepared using NEBNext UltraII DNA Library Prep Kit for Illumina (NEB, E7645) following manufacturers instructions. Briefly, fragmented DNA underwent 5′ phosphorylation and dA-Tailing to prepare the fragment ends for adapter ligation. Sample concentration was checked using Qubit dsDNA High Sensitivity (HS) kit (Thermo Fisher), to determine adapter dilutions. For input samples the adapters were not diluted, however a 1:25 dilution of adapters in 10 mM Tris-HCl pH 7.5, was performed for immunoprecipitation samples. A cleanup of the adapter ligation was performed using AMPure XP beads (Beckman Coulter) for size selection following the 200 bp protocol. PCR amplification was performed with 3 cycles of amplification for input samples, and 13 cycles of amplification for immunoprecipitation samples. A cleanup of the PCR reaction was performed using AMPure XP beads (Beckman Coulter), following protocol guidelines. Fragment sizes were checked before sequencing using the TapeStation (Agilent), using High Sensitivity DNA ScreenTape (Agilent).

Cleavage under targets and release using nuclease (CUT&RUN)

For CUT&RUN experiments, doxycycline inducible CBP-GFP, $CBP_{\Delta IDR6}$-GFP and $CBP_{\Delta IDR7}$-GFP cells were plated into 10 cm dishes and induced using the same concentrations of doxycycline as in ChIP experiments for 48 h 100,000 cells per reaction or input sample were harvested and DNA fragments were prepared using the CST CUT&RUN Assay kit according to the manufacturer's instructions. In brief, 100,000 cells per reaction were harvested, washed and bound to concanavalin A coated magnetic beads. Antibodies for each reaction were added (0.5 μg IgG: Rabbit (DA1E) IgG (CST, part of CUT&RUN assay kit); 1 μg H3K27ac: Histone H3K27ac (Active Motif)) and incubated overnight at 4°C. pAG-MNase was added to each tube and incubated for 1 h, then activated through the addiction of 3 mM $CaCl_2$ for 30 min at 4°C. Stop buffer was added, supplemented with 50 pg Spike-in DNA per sample (CST, part of CUT&RUN assay kit) and DNA fragments were eluted from the beads. DNA was then purified by phenol:chloroform extraction and ethanol precipitation and resuspended in 50 μL 1x TE buffer.

CUT&RUN library preparation

CUT&RUN DNA fragments were used to prepare libraries using the NEBNext Ultra II Library prep kit as described for ChIP-seq with the following changes. Adaptors were diluted for 1:10 for non-input samples and were cleaned up without size selection. Between 10 and 14 cycles of PCR were used for adaptor ligation dependent upon starting DNA concentration.

RNA-seq

RNA extraction

For RNA-seq doxycycline inducible CBP-GFP, $CBP_{\Delta IDR6}$-GFP and $CBP_{\Delta IDR7}$-GFP cells were plated into 10 cm dishes and induced using the same concentrations of doxycycline as described previously. RNA was extracted using TRIzol and chloroform, DNase treated to remove genomic DNA, then further purified with a subsequent phenol chloroform extraction and ethanol precipitation. RNA concentrations were measured using the broad range RNA Qubit kit (ThermoFisher).

RNA-seq library preparation

RNA-seq libraries were prepared using the Quant-seq 3′ mRNA-Seq Library Prep kit according to the manufacturer's instructions. In brief, 500 ng RNA was used per sample for cDNA synthesis, subsequent RNA removal and purification. qPCR was used to identify the optimal number of cycles for PCR amplification: between 16 and 23 depending upon sample (qPCR Add-on Kit, Lexogen) and the cDNA was then amplified accordingly, followed by purification of the libraries using magnetic beads.

Computational analysis

Identification of CBP-IDRs

To predict disordered regions in CBP, we used DISOPRED3[24] and PONDR[26] disorder prediction software. Tested CBP-IDRs were determined using PONDR VSL2 predictor, where stretches of amino acids that have a prediction of disorder above 50% were classed as intrinsically disordered regions. A mutant was also generated spanning the region where CBP binds to FUS we termed the CBP-FUS Interaction Domain (CFID).

Analysis of CBP sequence properties

NARDINI+. Sequence-level features of the target protein were analyzed using NARDINI+ (version 1.1)[28,29] implemented through a Colab Notebook. Analysis of Full length CBP_{WT} was done using the 'NARDINI+_from_accession' iPython notebook with Uniprot accession Q92793. IDRs identified by NARDINI were subsequently mapped to our CBP-IDRs identified using PONDR. In particular, 'IDR #1' from NARDINI+ was not identified by PONDR, as it was less than 50 amino acids in length; IDR #7 from NARDINI+ corresponded to CBP_{AL}. For individual IDR sequences and CBP shuffle mutant sequences, we implemented the 'NARDINI+_from_fasta' iPython notebook. The resulting quantitative *Z* score vectors were used to characterize the protein's molecular grammar and predict its functional roles.

localCIDER. Analysis of sequence properties was carried out using a local installation of localCIDER.[35] Linear composition plots for full length CBP_{WT} and CBP_{CFID} were calculated using a blob length window of 200 bp and 50 bp respectively.

PLAAC. PLAAC analysis was carried out using the web-based PLAAC server.[37]

Generating shuffle variants. Shuffle sequence variants were generated in GOOSE[36] using the 'Constant residues variant' option to randomly shuffle residues without changing the overall amino acid composition of the IDRs.

AlphaFold structure prediction (version 2.3.2). All structure predictions were performed using AlphaFold version 2.3.2[26] implemented through a Colab notebook. We used the monomer model with relaxation and specified five recycles. AlphaFold produces a per-residue confidence metric called predicted local distance difference test (pLDDT) on a scale from 0 to 100. pLDDT estimates how well the prediction would agree with an experimental structure; a pLDDT >70 is considered to correspond to a generally correct backbone prediction.[76] To assess the confidence of predictions carried out on CBP C-terminal domains (Figure S3E), we provided a duplicate view of our model colored by pLDDT score. All visualization was done using UCSF ChimeraX.[73]

QUANTIFICATION AND STATISTICAL ANALYSIS

Image analysis

Integrated intensity density

Before calculating the Integrated density, individual nuclei were isolated from a maximum projection and saved as. tif files where the file names were blinded using ImageJ/Fiji plugin: Blind Analysis Tool, File Name Encryptor.[58] These blinded files were categorized by two individuals independently, scoring the images as either diffuse, containing puncta, overexpressed or untransfected. Any nucleus that had a single puncta, was described as containing puncta; those that were transfected but displayed a diffuse signal were categorized as diffuse. Overexpressed nuclei were any nuclei where the signal intensity was too great to identify individual puncta, and untransfected cells were nuclei where little to no signal intensity was observed (Figure S2C). Both overexpressed and untransfected nuclei were removed from the dataset and an average percentage of nuclei which displayed either puncta or a diffuse phenotype was determined for each of the constructs.

To assess the punctate nature of the nuclei in an unbiased manner we also calculated the standard deviation of pixel intensity across the nucleus. Nuclei containing puncta would display a higher standard deviation between pixels compared to nuclei with a diffuse signal. A region of interest (ROI) was drawn around the nucleus by applying a manual threshold to isolate only the nuclei in ImageJ/Fiji. This region was applied to the raw image and the standard deviation was calculated within this region. All downstream analysis was done using R in Rstudio; significance *p* values for comparison of punctate signals were calculated using a Kruskal-Wallis test. Graphs and statistical testing was performed using R in RStudio.[59,60]

Integrated density, the intensity multiplied by the area, for each condensate produced by a defined construct was calculated in ImageJ/Fiji[57] using a custom macro. A maximum projection was generated from each z stack, and the condensates were identified by applying a manual intensity threshold to each image to generate a mask. The intensity threshold was internally consistent within each experimental repeat, where the threshold was chosen to best isolate condensates across the range of different phenotypes observed within the constructs tested. Within the mask, each independent ROI was labeled, and the area, Integrated Density, and circularity was measured for each ROI.

Once these images had been analyzed, the percentage of nuclei which contained a ROI which has an intensity higher than that of the set intensity threshold value was further calculated. This value was described as the transfection efficiency, and was generated to identify which nuclei had passed the threshold value. Filters were then applied sequentially to the data: 1) To exclude overexpressed nuclei, a maximum gray value of 10 was set; 2) To remove regions of high intensity that were too small to represent puncta, an area threshold (<3 pixels/0.36 μm) was applied; 3) To remove regions of overlapping puncta, a circularity threshold (<0.25) was set. All downstream analysis was done using R in Rstudio; significance *p* values for comparison of CBP-GFP behaviors (number of condensate per nuclei and integrated density) were calculated using a Kruskal-Wallis test. Graphs and statistical testing was performed using R in RStudio.

optoDroplet

A custom ImageJ macro was written to identify puncta formed in the mCherry channel. Images were run through an ImageJ plugin called Stack Registration (StackReg[58]), and a threshold was applied to generate a binary mask that underwent binary processing of closing followed by opening. For IDR1, IDR3, IDR4, AL, IDR6, IDR7 and the CFID the threshold was set using RenyiEntropy, and for IDR2 and IDR5 the Default setting was used. The parameters were then set in analyze particles, applying a size range of 50 - infinity, to generate ROIs which equated to the outline of the signal region, which was the nuclei. These ROIs were then applied to the original, raw image that underwent a multi-measure to calculate the standard deviation of the pixels within the nuclei over the time course. Regions found in the first frame were used to monitor the change in the standard deviation over the time course, where the average Fold Change was then calculated. A rate of change was then calculated over the time course based on the time at which the curve for the positive control (FUS) plateau. For IDR1, IDR3, IDR4, AL, IDR6, IDR7 and the CFID this was done over the first 32 s, whereas for IDR2 and IDR5 this was calculated over the first 72 s. For IDR1, IDR3, IDR4, AL, IDR6, IDR7 and the CFID the statistics for the rate of change were performed in GraphPad prism, where an unpaired students *t* test was used to determine statistical significance relative to the negative control. For the IDR2 and IDR5 statistics were performed using R in RStudio, using the Kruskal-Wallis test. Graphs for visualization were made using R in RStudio.

FRAP in CBP-HaloTag

Images for each FRAP time course were loaded into ImageJ/Fiji and processed using StackReg to remove drift in the sample. Over each time course, the intensity was calculated for a region of interest around the bleached area, before being corrected for

photobleaching over the time course using a reference region within the same nuclei. Relative intensity was calculated by subtracting the intensity at T = 0, where this was defined as the first frame after photobleaching, and then normalized to the pre-bleach intensity for each construct. Rate constants and T = ½ were calculated in GraphPad Prism 9, using a non-linear regression with settings one phase association with a variance weighting of $1/Y^2$.

FRAP in transfected cells

Time courses from FRAP of overexpressed protein were quantified using ImageJ/Fiji. The intensity was calculated over the time course, using a ROI of 0.22 μm, which is smaller than the condensate to only monitor the intensity within the condensate. The condensate was manually tracked throughout the time course, moving the ROI when the condensate moved. The relative fluorescence recovery was calculated by subtracting the intensity at T = 0, the first frame post bleaching and then normalized to the pre-bleach intensity for each construct. Rate constants and T = ½ were calculated as described for FRAP of CBP-HaloTag.

Quantification of CBP-HaloTag puncta data from the Zeiss Lattice Lightsheet 7 in the absence and presence of overexpressed CBP-GFP, $CBP_{\Delta IDR6}$-GFP, $CBP_{\Delta IDR7}$-GFP

Images were preprocessed in ImageJ/Fiji, where background was subtracted using a rolling ball of 50, and the images were sharpened. The preprocessed images were then converted to .sis files using Arivis SIS converter software before being quantified using Arivis Vision4D version 3.4. The data were first imported into the pipeline as a current time point. A denoise preset was run on either the Janelia Fluor channel for CBP-HaloTag only, or on the GFP channel in dual color images to isolate either all nuclei present or all transfected nuclei respectively. A discrete Gaussian of 5 μm was applied to this channel, to blur the edges of the nuclei, after the denoise the results were saved as a temporary document. Next an intensity threshold segmentor was applied to the denoised channel to isolate the nuclei of interest. For CBP-HaloTag only a threshold of 350 was applied, with a core filter of 400 and size range of 500 - 10,000 μm^2 was applied to isolate only nuclei. For overexpressed GFP constructs a threshold of 600 was applied, with a core filter of 1000 and size range of 500 - 10,000 μm^2 was applied. The blob finder was then applied to the Janelia Fluor channel for endogenous CBP-HaloTag in all cases. For CBP-HaloTag only a diameter of 5 μm was applied with a probability threshold of 22% and a split sensitivity of 50%. In the dual color images a diameter of 5 μm was applied with a probability threshold of 6% and a split sensitivity of 65% was applied. A segment feature filter was then applied to remove any objects that are too small to be classified as puncta. A compartment section was then applied to assign the condensates identified in the blob finder to the nuclei identified within the intensity threshold segmentor. The compartmentalization was selected as a full overlap so that only puncta contained within the nucleus was counted. The data were then exported as a Master-Details report, containing features of the nuclei and details of the condensates - these features included volume, area and intensity of puncta. Graphs for visualization were made using R in RStudio.

ChIP-seq data analysis

ChIP-seq samples were sequenced using paired-end 150 sequencing on an Illumina NovaSeq 6000 platform (Novogene). Raw data quality was assessed using FastQC v0.11.9(*Babraham bioinformatics - FastQC A quality control tool for high throughput sequence data*, n.d.) and adapters were trimmed using Cutadapt v3.4[61] implemented in Trim Galore (https://www.bioinformatics.babraham.ac.uk/projects/trim_galore/). Trimmed reads were aligned to human genome assembly GRCh38 using Burrows-Wheeler Alignment (BWA) v0.7.17-r1188.[62] For downstream analysis, replicates were merged and duplicate reads removed using Picard v2.27.4 (https://broadinstitute.github.io/picard/), before read quality filtering using SAMTools v1.15.1.[63] BigWig files were generated by normalizing per million reads mapped (RPM) and converting to bedgraph format with Bedtools v2.30.0,[64] then to BigWig format using UCSC utilities (bedGraphToBigWig v377.[65] ChIP-seq peaks were called on filtered data using MACS2 v2.2.7.1[67] using the BAMPE option and a broad peak cutoff of 0.001. All gene co-ordinates were obtained from Refseq. All initial processing, alignment and peak calling was completed as part of the Nextflow ChIP-seq pipeline v2.00[67] on the University of Sheffield High Performance Computing (HPC) cluster. Intersection of ChIP-seq peaks, calculation of relative distance plots[44] and Jaccard statistics[44] were done using Bedtools v2.31.0. For intersection with genome regions, intersection was made in the order Promoter (1kb window upstream of TSS) > Exons > Introns > Intergenic. Control peaks corresponding to each sample were calculated using bedtools shuffle, over a window restricted to 40kb upstream of transcription start sites on the same chromosome. Subsequent analysis was done using a local installation of DeepTools v3.5.5.[68] Read density coverage was calculated using multiBigwigSummary in 1kb bins over the entire genome; Correlation coefficients between samples were calculated using plotCorrelation; Heatmaps and metaplots displaying signals over a 5kb window aligned to peak centers were generated using computeMatrix and plotHeatmap; Read density enrichment over defined peak regions were calculated using plotEnrichment. All downstream analysis was done using R in Rstudio; significance *p* values for tag enrichment were calculated using a two-sided Mann-Whitney U test in R.[59] The high-throughput sequencing data from this publication have been deposited to the GEO database (https://www.ncbi.nlm.nih.gov/geo/) and assigned the identifiers GSE268266 (ChIP-seq) and grouped under SuperSeries GSE299618.

CUT&RUN data analysis

CUT&RUN sequencing data were processed and analyzed following a spike-in normalization strategy to enable quantitative comparisons across samples. Samples were sequenced using paired-end 150 sequencing on an Illumina NovaSeq 6000 platform (Novogene). Raw data quality was assessed using FastQC v0.11.9(*Babraham bioinformatics - FastQC A quality control tool for high throughput sequence data*, n.d.) and adapters were trimmed using Cutadapt v3.4 implemented in Trim Galore (https://www.bioinformatics.babraham.ac.uk/projects/trim_galore/). Trimmed reads were aligned to two distinct reference genomes: Homo

sapiens GRCh38 (Target genome) or S.cervisiae SacCer3 R64 (spike-in control genome) using bowtie2 v2.5.4[69] in very sensitive local alignment mode (–local –very-sensitive-local –no-unal –no-mixed –no-discordant -q -I 10 -X 700 –dovetail -x), before read quality filtering using SAMTools v1.15.1(Li et al., 2009). We used featureCounts v2.0.6[70] to generate a count matrix for each sample containing the total number of reads uniquely mapping to the spike-in genome. This was used to calculate a scaling factor for each sample using DEseq2 v1.40.2.[71] To enable direct quantitative comparison of signal intensity across samples, normalized BigWig files were generated in MACS3 v3.0.0b1. Firstly, we created bedgraph files using the callpeak function on MACS3, and then scaled by the previously calculated spike-in scaling factor. Normalized bedgraph files were then used to calculate the fold enrichment relative to the IgG background control. H3K27ac enriched peaks were called using MACS3. Peak intensity values from spike-in normalized BigWig files were then used for inter-sample comparisons and differential analyses using a local installation of DeepTools v3.5.3 as described previously for ChIPseq data. All sequencing data analyzed in this study have been deposited at NCBI's GEO database (https://www.ncbi.nlm.nih.gov/geo/) and assigned the identifier GSE299613 (CUT&RUN) and grouped under SuperSeries GSE299618.

RNA-seq data analysis

RNA-seq samples were sequenced using paired-end 150 sequencing on an Illumina NovaSeq 6000 platform (Novogene). Following sequencing, Read 2 was discarded and downstream data analysis was performed using only Read 1, according to manufacturer's recommendations for libraries prepared using the Quant-seq 3′ mRNA-Seq Library Prep kit. Raw data quality was assessed using FastQC v0.11.9(Babraham bioinformatics - FastQC A qu …) and adapters were trimmed using Cutadapt v3.4 (Martin 2011) implemented in Trim Galore (https://www.bioinformatics.babraham.ac.uk/projects/trim_galore/). Reads were aligned using STAR (v2.7.6)[72] allowing soft-clipping of read ends during alignment to generate a geneCounts matrix. This was then used as input for all downstream analysis in DESeq2 v1.40.2 in Bioconductor.[71] All sequencing data analyzed in this study have been deposited at NCBI's GEO database (https://www.ncbi.nlm.nih.gov/geo/) and assigned the identifier GSE299614 (RNA-seq) and grouped under SuperSeries GSE299618.

Statistical analysis

All statistical details can be found in figure legends and/or in figures, including statistical tests used and replicate information, and data visualization details. n represents biological replicates. Data are presented as mean ± SEM or mean ± SD, depending on the experiment from at least 3 independent biological replicates. Boxplots show median (center line), and the box limits represent the first and third quartiles. Whiskers extend to 1.5x the interquartile range and individual datapoints represent outliers. Statistical significance was determined based on the distribution and number of groups. Non-parametric data were analyzed by Mann-Whitney U test or Kruskal-Wallis test. Significance is indicated in the figure legends either by reporting absolute p values or by the following asterisk convention: $*p < 0.05$, $**p < 0.01$, and $***p < 0.001$. Non-significant differences are labeled as ''ns''. All statistical analyses were performed using GraphPad Prism or R in RStudio.''